

Core-Collapse Supernovae as Supercomputing Science: a status report toward 6D simulations with exact Boltzmann neutrino transport in full general relativity

Kei KOTAKE^{1,2}, Kohsuke SUMIYOSHI³, Shoichi YAMADA^{4,5},
Tomoya TAKIWAKI², Takami KURODA¹, Yudai SUWA⁶, and Hiroki NAGAKURA^{4,6}

¹*Division of Theoretical Astronomy, National Astronomical Observatory of Japan,
2-21-1, Osawa, Mitaka, Tokyo, 181-8588, Japan,*

²*Center for Computational Astrophysics, National Astronomical Observatory of
Japan, 2-21-1, Osawa, Mitaka, Tokyo, 181-8588, Japan*

³*Numazu College of Technology, Ooka 3600, Numazu, Shizuoka 410-8501, Japan*
ℰ

*Theory Center, High Energy Accelerator Research Organization (KEK),
Oho 1-1, Tsukuba, Ibaraki 305-0801, Japan,*

⁴*Science ℰ Engineering, Waseda University, 3-4-1 Okubo, Shinjuku, Tokyo,
169-8555, Japan*

⁵*Advanced Research Institute for Science and Engineering, Waseda University,
3-4-1 Okubo, Shinjuku, Tokyo, 169-8555, Japan*

⁶*Yukawa Institute for Theoretical Physics, Kyoto University, Oiwake-cho,
Kitashirakawa, Sakyo-ku, Kyoto, 606-8502, Japan*

This is a status report on our endeavor to reveal the mechanism of core-collapse supernovae (CCSNe) by large-scale numerical simulations. Multi-dimensionality of the supernova engine, general relativistic magnetohydrodynamics, energy and lepton number transport by neutrinos emitted from the forming neutron star as well as nuclear interactions there, are all believed to play crucial roles in repelling infalling matter and producing energetic explosions. These ingredients are nonlinearly coupled with one another in the dynamics of core-collapse, bounce, and shock expansion. Serious quantitative studies of CCSNe hence make extensive numerical computations mandatory. Since neutrinos are neither in thermal nor in chemical equilibrium in general, their distributions in the phase space should be computed. This is a six dimensional (6D) neutrino transport problem and quite a challenge even for those with an access to the most advanced numerical resources such as the “K computer”. To tackle this problem, we have embarked on multi-front efforts. In particular we report in this paper our recent progresses in the treatments of multi-dimensional (multi-D) radiation-hydrodynamics. We are currently proceeding on two different paths to the ultimate goal; in one approach we employ an approximate but highly efficient scheme for neutrino transport and treat 3D hydrodynamics and/or general relativity rigorously; some neutrino-driven explosions will be presented and comparisons will be made between 2D and 3D models quantitatively; in the second approach, on the other hand, exact but so far Newtonian Boltzmann equations are solved in two and three spatial dimensions; we will show some demonstrative test simulations. We will also address the perspectives of exa-scale computations on the next generation supercomputers.

§1. Explorations of CCSNe by multi-D simulations

From the very beginning,¹⁾ CCSN research has been one of the greatest challenges in computational astrophysics. This is simply due to the following facts (see,

e.g., 2), 3) and references therein): 3D macroscopic magnetohydrodynamics on stellar scales is largely dictated by weak/strong interactions on femto-meter scales; not only dynamical time scales of milliseconds but neutrino-diffusion time scales of $\gtrsim 100$ ms become also important in the dynamics of massive star cores; compactness of proto-neutron stars (PNSs) and high velocities of collapsing material make it simply impossible to neglect special/general relativity; (magneto)hydrodynamical instabilities render the core dynamics intrinsically non-spherical; phase transitions in dense hadronic matter and/or neutrino oscillations may have a critical impact. These diverse physical elements involved in CCSNe, although they are the reasons why many researchers from different disciplines have been attracted so much, are the very sources of difficulties in numerical simulations.

Energetics also suggests the subtlety in the explosion dynamics. Recently advancing ability of the HST has enabled the direct observation of the progenitors of nearby CCSNe from pre-explosion images (see⁴⁾ for review). The accumulating observations suggest that the majority of CCSNe (the so-called type II-plateau (II-P)) comes predominantly from stars in the range about of 8 - 16 M_{\odot} .⁴⁾ A generic explosion energy for the progenitors in the mass range is roughly on the order of 10^{51} erg,⁵⁾ which is much smaller than the available energy, $\sim 10^{53}$ erg, i.e., the gravitational binding energy of PNSs. This large amount of energy is stored as the internal energy of PNSs and tapped slowly by neutrinos. After the successful detections of neutrinos from SN1987A followed by detailed analyses of these events (e.g., 6), and see also 7) for a recent review), CCSN researchers have a confidence that the explosion energy is indeed supplied by this reservoir. Present state-of-the-art supernova simulations require more than 10^{18} operations and typically more than several months for a single model on currently available best supercomputing platforms. The energy conservation should be satisfied within an error of at least less than $\sim 1\%$ ($= 10^{51}$ erg/ 10^{53} erg) in such very long-term simulations to obtain reliable results. It may not be difficult then to imagine how demanding the numerical simulations of CCSNe are.

It is interesting that after +45 years of intensive and extensive theoretical studies we are still working on the same scenario that Colgate and White (1966) envisaged in their seminal paper,¹⁾ in which they reported the first CCSN simulation. The abstract of their paper ended with the sentence, "*The energy release corresponds to the change in gravitational potential of the unstable imploding core; the transfer of energy takes place by the emission and deposition of neutrinos*". As is now well known, this is exactly the essence of the so-called neutrino-heating mechanism (e.g., 8) for review). Although they proposed originally that the mechanism works promptly after bounce, Bethe and Wilson later amended it^{9), 10)} to the currently prevailing form, in which a bounce-generated shock wave is stalled first, but revived later by the deposition of neutrinos and an explosion follows in several hundred milliseconds after bounce. The scenario was investigated intensively for the first 5 years in the new millennium under the assumption of spherically symmetry but with the full Boltzmann treatment of neutrino transfer.¹¹⁾⁻¹⁴⁾ General relativity^{12), 14)} and/or various neutrino reactions, some of which are supposed to be of minor importance,¹⁵⁾⁻¹⁷⁾ were also implemented.

These explorations made clear, however, that the neutrino-heating mechanism fails to produce explosions in 1D spherical symmetry except for super-AGB stars at the low-mass end.¹⁸⁾ Not deterred by this failure, researchers changed gear to multi-D modeling. By this time there had already been mounting observational evidence that supernova explosions are indeed aspherical in general (see, e.g., 19)–21) and references therein). Numerical experiments also suggested that breaking spherical symmetry holds a key to success of the neutrino-heating mechanism; convective motions (e.g., 22)–26)) and/or the so-called standing accretion shock instability, or SASI, (e.g., 27)–35) and references therein) help the onset of neutrino-driven explosions.

In the following years, we have indeed witnessed some exploding models by the neutrino-heating mechanism in axisymmetric 2D simulations (see, e.g., table 1 in 3)). Employing one of the best approximations for 2D neutrino transfer, Buras et al.³⁶⁾ reported explosions firstly for a non-rotating low-mass ($11.2M_{\odot}$) progenitor³⁷⁾ and then for a $15M_{\odot}$ progenitor³⁸⁾ with a moderate rotation being imposed.³⁹⁾ Implementing a multi-group flux-limited diffusion algorithm to their CHIMERA code in a ray-by-ray manner, on the other hand, Bruenn et al.⁴⁰⁾ obtained explosions for non-rotating progenitors³⁷⁾ in the mass range from $12M_{\odot}$ to $25M_{\odot}$. Implementing the ray-by-ray isotropic diffusion source approximation (IDSA)⁴¹⁾ in the ZEUS code with a reduced set of weak interactions, Suwa et al.⁴²⁾ pointed out that a rapidly rotating $13M_{\odot}$ progenitor produced a stronger explosion than the non-rotating counterpart did.⁴³⁾

Accompanying these successes are new questions, however. In addition to the apparent contradictions among the groups (see Table 1 in 3)), the models mentioned above produced generically under-energetic explosions at the end of simulations, with the diagnostic explosion energy being smaller by one or two orders of magnitude than the canonical kinetic energy of supernova ejecta ($\sim 10^{51}$ erg). Hence, it is a legitimate concern whether we can obtain energetic explosions comparable to observations by the neutrino-heating mechanism with appropriate nucleosynthetic yield, which is one of the most important observables.⁴⁴⁾ In the above-mentioned computations, the softest version of Lattimer & Swesty’s (LS) equation of state (EOS)⁴⁵⁾ with an incompressibility at nuclear density, K , of 180 MeV, was commonly employed. In addition to the fact that recent experiments suggest a stiffer EOS with $K = 240 \pm 20$ MeV,⁴⁶⁾ it is now thought to be a serious flaw that the LS180 EOS cannot support a $2M_{\odot}$ cold neutron star that is certainly existent in the universe^{47)*)}. Employing a stiffer EOS with $K = 263$ MeV based on the Hartree-Fock approximation,⁵⁰⁾ Marek et al.³⁹⁾ found no explosion for the same progenitor model, whereas they indeed obtained an explosion for the Shen’s EOS that is even stiffer with $K = 281$ MeV.⁵¹⁾ Suwa et al. also pointed out that not only the incompressibility but the symmetry energy also matters for the success of neutrino-driven explosions.⁵²⁾ Impacts of more detailed properties of nuclear EOSs (such as the density dependence of symmetry energy and the skewness of compressibility^{53),54)}) on the multi-D neutrino-heating mechanism are remaining to be understood.

*) The maximum mass for the LS180 EOS is about $1.8M_{\odot}$ (see, e.g., 48),49)).

The paramount interest of supernova researchers at present is 3D effects, however. We know in fact that SASI is qualitatively different between 2D and 3D^{33),55)} and it is naturally expected that this may have some consequences to success of the neutrino-heating mechanism in 3D. So far experimental simulations are contradicting each other: Nordhaus et al.⁵⁶⁾ claimed that 3D dynamics will make shock revival easier than 2D. The assertion was challenged later by Hanke et al.,⁵⁷⁾ who found little difference in the critical neutrino luminosity for shock revival between their 2D and 3D simulations. In both of the experimental computations, the neutrino transfer was not solved and the controversy will be settled only by detailed self-consistent 3D simulations. In the next section, we present our recent findings that illuminate 3D effects on the neutrino-driven mechanism. The former part of §2 is devoted to our 3D Newtonian hydrodynamical simulations with spectral neutrino transport whereas in the latter half we show the latest results of our fully general relativistic (GR) 3D simulations that employ a more approximate neutrino transport scheme.

Although we will focus on the neutrino-heating mechanism in this paper, it should be mentioned here that there are some other viable mechanisms. In the so-called acoustic mechanism,⁵⁸⁾ oscillations of PNSs are supposed to produce pressure perturbations and send acoustic powers to the stalled shock until it revives and produces an explosion. The mechanism will then be particularly important in the later postbounce phase, when the neutrino luminosity has already declined and the neutrino-heating mechanism has no chance of success. The merit of this mechanism is that matter accretion, the source of acoustic powers, will last long, possibly until the shock is revived. The scenario was challenged by Quataert et al.,⁵⁹⁾ however, who demonstrated that the amplitudes of g-mode oscillations of PNSs will not be so large (see also 60)). Although the additional energy input by acoustic waves is very appealing, it still remains an issue under vivid debates and has yet to be confirmed by other groups.³⁹⁾ The magnetohydrodynamical (MHD) mechanism taps rotational energies of stellar cores (e.g., 61)–73), 75). See also 2) for collective references). Magnetic fields are expected to be amplified spontaneously by the magneto-rotational instability (MRI) even if they are tiny prior to collapse.⁷⁶⁾ This mechanism requires rapid rotation of stellar cores at the onset of core collapse.⁷⁶⁾ Recent stellar evolution models predict that such a condition can be realized only in the special case that experiences the so-called chemically homogeneous evolution^{77),78)} and applies to just a fraction ($\sim 1\%$) of massive stars. Further investigations are currently hampered by the fact that high numerical resolutions are required to accurately compute the growth of the MRI.^{79),80)} We finally list other possibilities proposed in the literature: exotic physics in the proto-neutron star,^{81)–83)} viscous heating by MRI,^{84),85)} and dissipation of Alfvén waves.⁸⁶⁾

Improvements of input physics are another important ingredient in the CCSN simulations. One of the authors provided an EOS table to the society,^{87)–89)} which is referred to as Shen’s EOS and is based on the relativistic mean field theory and Thomas-Fermi approximation and is now a standard choice for core-collapse simulations. Besides this and another representative EOS by Lattimer & Swesty,⁴⁵⁾ new sets of EOS’s have been reported recently.^{90)–92)} We have joined this effort to expand the inventory of EOS’s both above and below nuclear density for the last

few years. Above saturation density, we have later included hyperons in the same framework.⁹³⁾ We have also combined the original table with an EOS for quark matter, adopting the MIT bag model and the Gibbs condition for the first order phase transition.⁹⁴⁾ These modifications manifest themselves at high densities and will be more important for CCSNe with black hole formations than those with neutron star formations. It is emphasized that the EOS at high densities can be probed by neutrino and/or gravitational wave signals from core-collapse events.^{48),95)–97)} The EOS below nuclear saturation density is no less important. In the conventional EOSs,^{45),87)–89)} the so-called single nucleus approximation was employed, in which thermally populated heavy nuclei are represented by a single, supposedly the most abundant nucleus. Combining experimental nuclear mass data and a mass formula, we have solved Saha-like equations to obtain populations of various nuclei in constructing the EOS.⁹¹⁾ In doing so, not only the excluded-volume effect but the emergence of pasta phases as well as the modifications of bulk, Coulomb and surface energies by surrounding nucleons and nuclei are also taken into account phenomenologically. We are currently preparing an EOS table including the electron capture rates according to the obtained populations.⁹⁸⁾ Detailed comparisons with other tables^{90),99)} will be also published soon.

The ultimate goal of CCSN simulations is 3D neutrino-radiation-(magneto-) hydrodynamics in full GR, in which the exact Boltzmann equations are solved and all the relevant weak interactions are included with sufficient realism. It is worth mentioning that more massive stars than the SN II-p mentioned earlier are expected to lose much of their mass and explode as hydrogen-stripped SNe (Ib/c and IIb). Among them, the type Ic-BL SNe, which are associated with long gamma-ray bursts,¹⁰⁰⁾ all show much broader lines than SNe Ic. Due to the large kinetic energies of $2 - 5 \times 10^{52}$ erg, they have been referred to as "hypernovae" (e.g., Ref.¹⁰¹⁾ for a recent review), the central engine of which is likely to be associated with massive stellar core-collapse with black-hole formation (e.g., collapsar, see collective references in Refs.^{191),192)}). In such a system, the implementation of full GR in numerical simulations is essential. In one of our approaches mentioned above, 3D hydrodynamics in full GR is first addressed in §2 with neutrino transport being approximated one way or another. On the other front, we are pursuing the Boltzmann transport in 3D first. We present the current status of our efforts along this path in §3. Our method is based on an implicit finite differencing of the Boltzmann equations and the inversion of large matrices in a very efficient way is one of the major challenges. As discussed in the final section, the 3D version of the code may work only on the next generation, exa-scale platforms. In this sense, what we provide in the following sections is just a snapshot of a long, on-going documentary film that will record our struggles to make the "dream simulation" come true.

§2. 3D hydrodynamical simulations with approximate neutrino transport

2.1. 3D Newtonian simulations with spectral neutrino transport

It is generally very computationally expensive to solve neutrino transport in 3D and a light-bulb scheme¹⁰²⁾ has been widely used so far, in which neutrino heating and cooling are treated in a parametric manner to trigger 3D explosions. Using this prescription, Nordhaus et al.⁵⁶⁾ was the first to argue that the critical neutrino luminosity for producing neutrino-driven explosions becomes significantly smaller in 3D than in 2D (see, however, 57)). They employed the CASTRO code with an adaptive mesh refinement technique, by which unprecedentedly high resolution 3D calculations were made possible.

Since the light-bulb scheme can capture fundamental properties of neutrino-driven explosions (albeit on a qualitative basis), it is one of the most prevailing approximations adopted in recent 3D models (e.g., 32), 33), 103)). A number of important findings have been reported recently in these simulations, such as a potential role of non-axisymmetric SASI flows in generating spins (see 103), 104) as well as 55), 105)) and magnetic fields¹⁰⁶⁾ of pulsars, stochastic nature of gravitational-wave (e.g., 3), 107), 108)) and neutrino emission (see 109) for recent review).

To go up the ladders beyond the light-bulb scheme, we studied 3D effects on the supernova mechanism by performing the first 3D, multi-energy-group, radiation-hydrodynamical core-collapse simulations.¹¹⁰⁾ For the spectral transport, the IDSA scheme is implemented, which can be done rather in a straightforward manner by extending our 2D modules^{42), 52)} to 3D. This can be made possible because we apply the so-called ray-by-ray approach (e.g., 36)) in which the neutrino transport is solved along a given radial direction by assuming the angle-averaged matter distribution in a spherically symmetric manner. From a technical point of view, it is worth mentioning that the ray-by-ray treatment is highly efficient in paralellization^{*)} on present supercomputers, most of which employ the message-passing-interface (MPI) routines. The IDSA scheme splits the neutrino distribution into two components, each of which is solved with different numerical techniques (see 41) for more details). A drawback in the current version of the IDSA scheme is that heavy lepton neutrinos (ν_x , i.e., ν_μ , ν_τ and their anti-particles) as well as the energy-coupling weak interactions have yet to be implemented. The approximation level of the IDSA scheme is basically the same as the one of the Multi-Group Flux-Limited Diffusion MGFLD scheme. The main advantage of the IDSA scheme is that the fluxes in the transparent region can be determined by the non-local distribution of sources rather than the gradient of the local intensity like in MGFLD. In the following, we briefly summarize the main results on our 3D simulations, in which we obtained a first 3D explosion for an $11.2 M_\odot$ star.³⁷⁾

^{*)} along each radial ray

2.1.1. 3D dynamics from core-collapse through postbounce turbulence till explosion

Figure 1 shows three snapshots, which are helpful to characterize hydrodynamic features in 3D simulations. The top panel corresponds to $t = 15$ ms after bounce, showing that the bounce shock stalls (indicated by inward arrows in the top right panel) at a radius of 150 km. Note that the colors of velocity arrows are chosen so that they would change from yellow to red as the absolute values become larger. Looking carefully at the top right panel, we find that matter flows supersonically (indicated by reddish arrows) into the standing shock (the central transparent sphere), and then advects subsonically (indicated by yellowish arrows) onto the proto-neutron star (PNS, the central bluish region in the top left panel). For the non-rotating progenitor, the dynamics of collapsing iron core proceeds perfectly spherically till the stall of the bounce shock. This is the reason why multi-D effects are invisible in the entropy (top left panel) and density (top right panel) distributions right after bounce.

The middle panels show the epoch ($t = 65$ ms) when the neutrino-driven convection is already active. From the right panel, turbulent motions can be seen (arrows in random directions) inside the standing shock, which is indicated by the boundary between red and yellow arrows. The entropy behind the standing shock becomes high by the neutrino-heating (reddish regions in the left panel). The size of neutrino-heated hot bubbles becomes larger in a non-axisymmetric way later on, which is indicated by smaller structures encompassed by the stalled shock (i.e., inside the central greenish sphere in the left panel).

The bottom panels ($t = 125$ ms) show the epoch when the revived shock is expanding aspherically, which is indicated by the outgoing yellowish arrows in the right panel. The asphericity of the expanding shocks could be more clearly visible by the sidewall panels. From the entropy distribution (left panel), the expanding shock is shown to touch a radius of ~ 500 km (the projected back bottom panel). Inside the expanding shock (enclosed by the greenish membrane in the left panel), the bumpy structures of the hot bubbles are seen. In contrast to these smaller asphericities, the deformation of the shock surface is mild. This is a consequence of SASI, leading to the shock deformation dominated by low spherical-harmonics modes ($\ell = 1, 2$).

Figure 2 shows the net neutrino heating rate (left panel) and $\tau_{\text{res}}/\tau_{\text{heat}}$: the ratio of the residency time scale to the neutrino-heating time scale (right panel) for the snapshot of $t = 125$ ms in Fig. 1. This time scale ratio is known to be a useful quantity to diagnose the success ($\tau_{\text{res}}/\tau_{\text{heat}} \gtrsim 1$, i.e., the neutrino-heating timescale is shorter than the dwell time scale of material in the gain region^{*)} or failure ($\tau_{\text{res}}/\tau_{\text{heat}} \lesssim 1$) of the neutrino-driven explosion (e.g., 34), 84), 111), 112)). The left panel of Fig. 2 shows that there forms the so-called gain region, in which the neutrino heating dominates over cooling (seen as reddish regions in the wall panels). As seen in the right panel, the time scale ratio reaches ~ 2 in the gain region, the evidence that the shock-revival is driven by the neutrino-heating mechanism.

^{*)} where the neutrino heating dominates over the neutrino cooling (see Ref¹¹²⁾ for more detail).

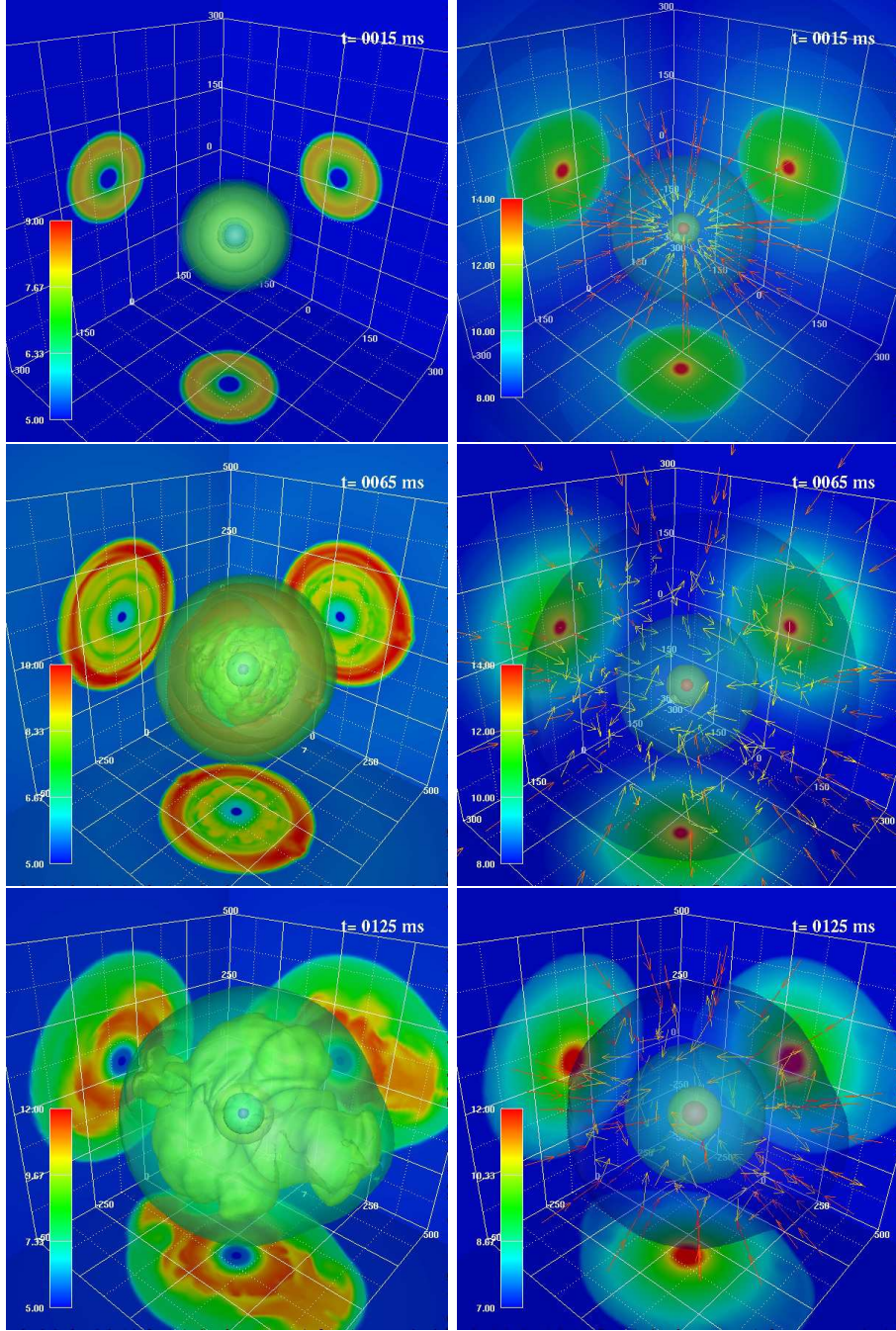


Fig. 1. 3D plots of entropy per baryon (left panels) and logarithmic density (right panels, in unit of g/cm^3) for three snapshots (top; $t = 15$ ms, middle; $t = 65$ ms, and bottom; $t = 125$ ms after bounce ($t \equiv 0$)) during the evolution of a (non-rotating) exploding 3D model of a $11.2 M_{\odot}$ star (figures taken from 110)). In the right panels, velocities are indicated by arrows. The color contours in the $x = 0$ (back right), $y = 0$ (back bottom), and $z = 0$ (back left) planes are projected on the sidewalls of the graphs. For each snapshot, the linear scale is shown along the axis in unit of km (figures taken from 110), reproduced by permissions of the AAS).

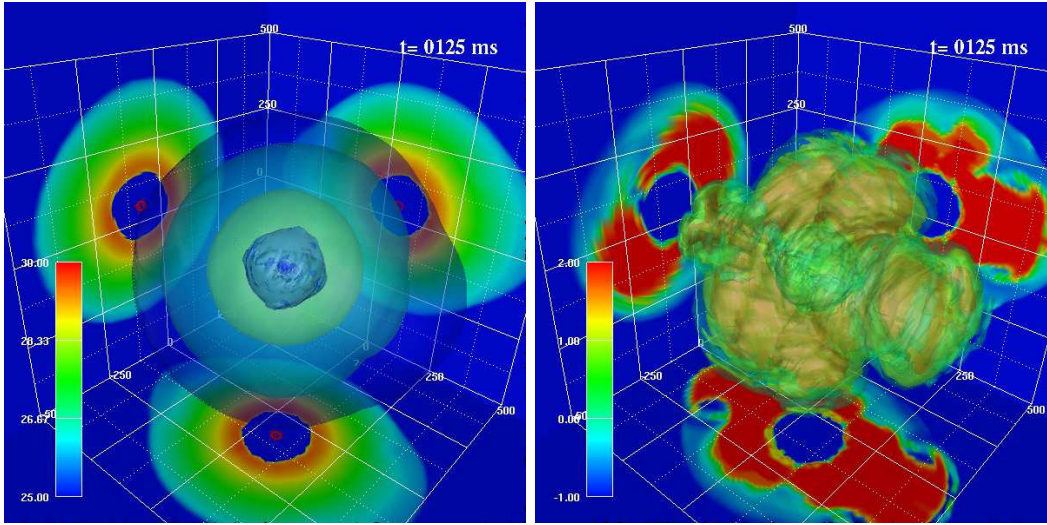


Fig. 2. Same as Figure 1 but for the net neutrino heating rate (left panel, logarithmic in unit of $\text{erg}/\text{cm}^3/\text{s}$) and $\tau_{\text{res}}/\tau_{\text{heat}}$ (right panel), which is the ratio of the residency to the neutrino heating time scales (see the text for details). The gain region (colored in red in left panel), in which neutrino heating dominates over cooling, is shown to be formed. The right panel shows that the condition of $\tau_{\text{res}}/\tau_{\text{heat}} \gtrsim 1$ is satisfied behind the globally aspherical shock, which is a characteristics of SASI (figures taken from 110), reproduced by permissions of the AAS).

2.1.2. 2D vs. 3D: which is more advantageous for the neutrino-driven explosion?

The left panel of Fig. 3 shows the comparison of mass-shell trajectories between the 3D (red lines) and corresponding 1D models (green line). At around 300ms after bounce, the average shock radius for the 3D model exceeds 1000km. On the other hand, no explosion is obtained for the 1D model. The right panel of Fig. 3 shows a comparison of the average shock radii as a function of the postbounce time. In the 2D model, the shock expands rather continuously after bounce. These trends in the 1D and 2D models are qualitatively consistent with those found in 36)*).

Comparing the shock evolutions between the 2D (green line in the right panel of Fig. 3) and 3D (red line) models, we find that the shock expands much faster in 2D. The pink line labeled by "3D low" is the result of the low resolution 3D simulation, in which the azimuthal grid number is reduced to half the number for the standard model. Note that the 3D computational grid consists of 300 logarithmically spaced radial zones and 64 polar (θ) and 32 azimuthal (ϕ) uniform mesh points to cover the entire sphere with a radius of 5000km. Compared with the standard 3D model (red line), the shock expansion is less energetic for the low resolution model (later than $\sim 150\text{ms}$). These results indicate that a successful explosion is most easily obtained in 2D and hampered by low resolutions. At first glance, this may be at odds with

*) The reason why the shock of our 2D model expands on average much faster than theirs might be our neglect of general relativity, inelastic neutrino-electron scattering and cooling by heavy-lepton neutrinos. All of these important missing ingredients in our 3D simulations could give a more optimistic condition for explosions. Apparently these ingredients should be appropriately implemented, which we hope to be tractable in the next-generation 3D simulations.

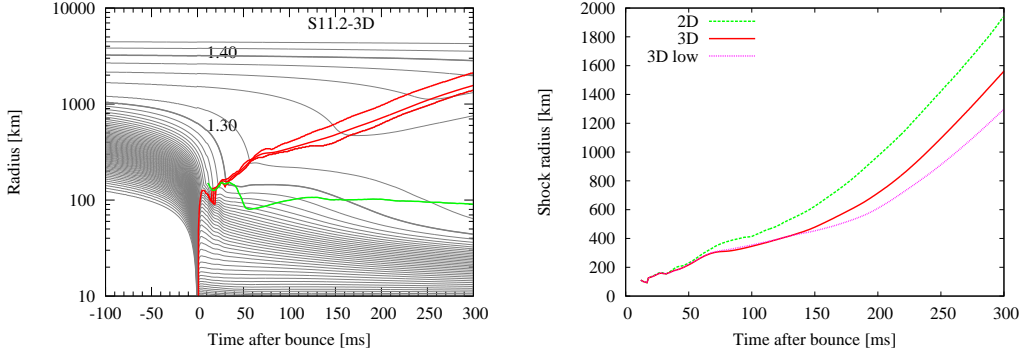


Fig. 3. Left panel: the time evolution of 3D model, visualized by mass shell trajectories in thin gray lines. Thick red lines show the positions of shock: the maximum (top), average (middle) and minimum (bottom) radii. The green line represents the shock position for the 1D model. The numbers "1.30" and "1.40" indicate the masses in unit of M_{\odot} that are enclosed inside each mass-shell. Right panel: the evolution of average shock radii for the 2D (green line) and 3D (red line) models. The pink line presents the low resolution 3D model, in which the azimuthal grid number is reduced to half the number for the standard model (see the body). Figures are taken from 110) (reproduced by permissions of the AAS).

the results obtained in the parametric 3D explosion models (e.g., 56)), in which the authors claimed that explosions would be easier in 3D than in 2D. The reason for the discrepancy is summarized shortly.

Fig. 4 compares the blast morphologies in the 3D (left panel) and 2D (right) models. In the former, non-axisymmetric structures are clearly seen. Performing a tracer-particle analysis, we find that the maximum residency time is longer in 3D than in 2D owing to the non-axisymmetric motions (see Fig. 5). This is one of advantageous aspects of 3D models to obtain the neutrino-driven explosions. Another merit in 3D is that convective matter motions below the gain radius is much more violent than in 2D, which enhances the neutrino luminosity in 3D (see 110) for more details). The negative point, on the other hand, is lower energies of emitted neutrinos owing to the enhanced cooling. The competition of these effects eventually leads to a longer neutrino-heating time scale in our 3D models with an outcome of a smaller net-heating rate compared with the corresponding 2D model (Fig. 6). Note here that the IDSA scheme, with which the feedback from the mass accretion to the neutrino luminosity is automatically and self-consistently incorporated unlike the light-bulb approximation that assumes a constant luminosity, is quite efficient and a good choice for the first-generation 3D simulations.

Although it is encouraging that the shock expansion becomes more energetic with better resolution (recall that the explosions obtained so far are all under-energetic³⁾ and the present model is no exception), this implies that a systematic and time consuming convergence test is required to draw a robust conclusion (e.g. 57)). More advanced treatments of neutrino transport as well as of gravity will be also needed, which will probably be a subject done on forthcoming petaflops-class supercomputers.

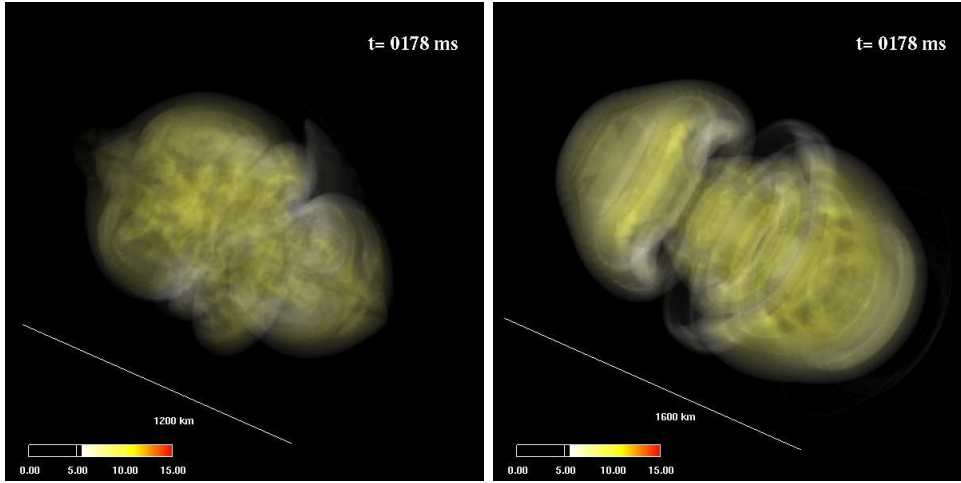


Fig. 4. Blast morphologies at $t = 178\text{ms}$ after bounce in our 3D (left) and 2D (right) models presented as the volume rendering of entropy. The progenitor is a $11.2M_{\odot}$ star.³⁷⁾ The polar axis is tilted by about $\pi/4$ in both panels (figures taken from 110), reproduced by permissions of the AAS).

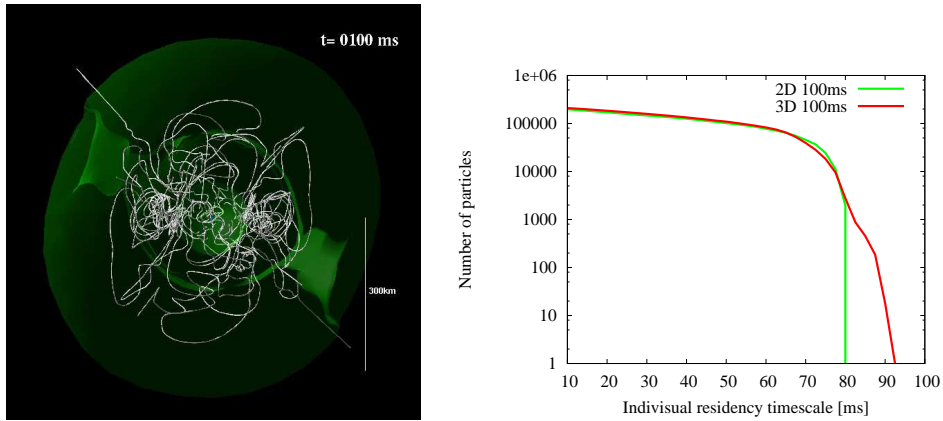


Fig. 5. Left panel: streamlines of selected tracer particles advecting through the shock to the PNS in the 3D model. The observer is located on the polar axis. Several surfaces of constant entropy are also displayed. An outer greenish one marks the shock surface whereas the PNS is presented as a central sphere. The linear scale is given at the bottom right corner. Right panel: the number of tracer-particles traversing the gain region as a function of their individual residency time for the 2D and 3D models given at $t = 100\text{ms}$ after bounce. The maximum residency time in the 3D model is longer than that in the corresponding 2D model (figures taken from 110), reproduced by permissions of the AAS).

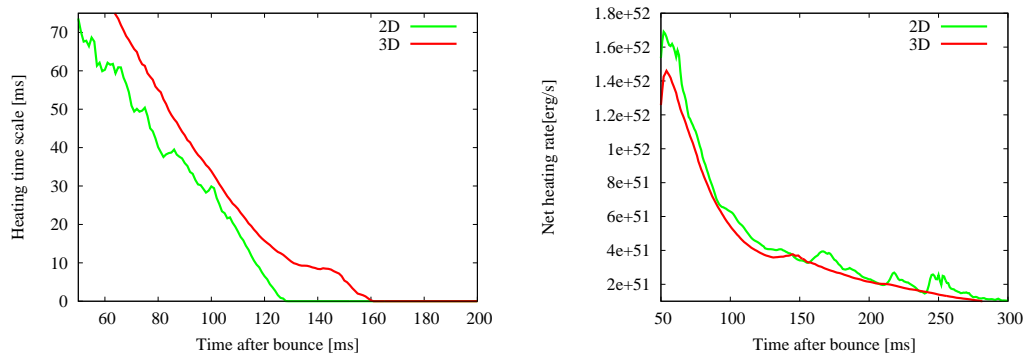


Fig. 6. Time evolutions of neutrino-heating time scale (left) and volume-integrated net neutrino-heating rate (right) in the 2D (green line) and 3D (red line) models (figures taken from Ref.,¹¹⁰ reproduced by permissions of the AAS).

2.2. 3D fully general relativistic simulations with an approximate neutrino transport

In addition to the 3D effects mentioned in the previous section, impacts of GR on the neutrino-heating mechanism stand out among the biggest open questions in the supernova theory. It should be remembered that researchers in the pioneering era of supernova simulations tackled GR from very early on,¹¹³⁾ using a newly derived formulation.¹¹⁴⁾ One year after Colgate & White published their seminal paper¹⁾, Schwartz¹¹⁵⁾ reported the first fully GR simulation of stellar collapse to study the supernova mechanism, implementing a gray neutrino transport in the 1D GR hydrodynamics code^{*}). Using the GR Boltzmann equations derived by Lindquist,¹¹⁶⁾ Wilson¹¹⁷⁾ developed a 1D GR-radiation-hydrodynamics code including more realistic (at that time) descriptions of the collisional term than the one adopted by Schwartz.¹¹⁵⁾ 1D GR hydrodynamical simulations with the so-called leakage scheme for neutrino cooling were also performed to explore hydrodynamical properties up to the prompt-shock stagnation.^{118)–120)} These pioneering studies, albeit with a much more simplified neutrino physics than today, did provide a bottom-line of our current understanding of the supernova mechanism (see Bruenn et al.¹²¹⁾ for a complete list of references for the early GR studies). In the middle of the 1980s, Bruenn¹²²⁾ developed a code that coupled 1D GR hydrodynamics to the MGFLD transport with a relativistic correction of order (v/c) and included the so-called standard set of neutrino interactions. By the late 1990s, the ultimate 1D simulations, in which the GR Boltzmann transport is coupled to 1D GR hydrodynamics, became feasible.^{12), 14), 121), 123)–126)}

Bruenn et al.¹²¹⁾ demonstrated clearly that the average neutrino energies of all neutrino flavors are higher in GR than in Newtonian gravity during the shock-heating phase. They also pointed out that the redshift and gravitational time dilation, the agents to counteract, are rather minor. Employing the best weak interaction rates available at present, Lentz et al.¹²⁷⁾ reported very recently the update of Bruenn et al.,¹²¹⁾ in which they showed that the neglect of the observer corrections in the transport equation particularly does harm to neutrino-driven explosions. In these full-fledged 1D simulations, a commonly observed disadvantageous aspect of GR is that the residency time of material in the gain region is shorter owing to stronger gravitational pull. All these effects taken into account, GR is negative in the neutrino-heating mechanism in 1D. In fact, switching from Newtonian to GR hydrodynamics, we find that the maximum shock radius becomes $\sim 20\%$ smaller in the postbounce phase (e.g., 127)).

In the most advanced multi-D simulations with spectral neutrino transport mentioned earlier, GR effects are addressed at best by a modified gravitational potential that is adopted from the 1D post-Newtonian correction.^{36), 39), 40), 128)} A possible drawback of this prescription is that the total-energy conservation is compromised

^{*}) Cited from his paper, "In this calculation, the neutrino luminosity of the core is found to be 10^{54} erg/s, or 1/2 a solar rest mass per second !! This is the mechanism which the supernova explodes". The neutrino luminosity rarely becomes so high in modern simulations, but it is surprising that the potential impact of GR on the neutrino-heating mechanism was already indicated in the very first GR simulation.

owing to the term added artificially to the Poisson equation for self-gravity. Since the supernova engine is powered by the gravitational energy, we have to avoid any potential inaccuracies in energy conservation. On the other hand, there have been a number of fully general relativistic simulations of massive star collapse thus far both in 2D (e.g., 129)) and in 3D (e.g., 130), 131), and references therein). The so-called conformal-flatness approximation (CFC) has been also employed.^{132),133)} In these computations the treatment of neutrino transport was overly compromised, e.g., with the transfer being entirely replaced by a prescribed Y_e formula¹³⁴⁾ or the so-called leakage scheme being adopted.^{135),136)*)}

In this section, we present results from our first generation multi-D hydrodynamical simulations in full GR that incorporate an approximate neutrino transport.¹³⁹⁾ The code is a marriage of an adaptive-mesh-refinement (AMR), conservative 3D GR MHD code developed by Kuroda and Umeda,¹⁴⁰⁾ and the approximate neutrino transport code that we newly developed in this work. Our GR code is based on the Baumgarte-Shapiro-Shibata-Nakamura (BSSN) formalism.^{141),142)} Hydrodynamics can be solved either in full GR or in special relativity (SR), a feature that allows us to investigate purely GR effects on the supernova dynamics. Using the so-called M1 closure scheme with an analytic variable Eddington factor, we solve the radiation energy and momentum. This part of the code is partially based on the Thorne’s momentum formalism,¹⁴³⁾ which was recently extended by Shibata et al.¹⁴⁴⁾ so that it should be more suitable for neutrino transport. To simplify the source terms of the transport equations, on the other hand, a multi-flavour neutrino leakage scheme is also employed partially. The new code is designed so that it could evolve the Einstein equation and GR radiation-hydrodynamical equations self-consistently, satisfying the Hamiltonian and momentum constraints. The AMR technique implemented in the 3D code enables us to follow the dynamics from the onset of gravitational core-collapse of a $15 M_\odot$ star through bounce up to ~ 100 ms after bounce in this study. We compute four models with different combinations of SR/GR and 1D/3D, which we label as 1D-SR, 1D-GR, 3D-SR and 3D-GR, respectively. Limited to the early postbounce phase ($t \lesssim 100$ ms), we discuss exploratory results in the following sections to illuminate GR effects in the multi-D neutrino-heating mechanism.

2.2.1. Hydrodynamical features in full GR 3D simulations

Four snapshots in Fig. 7 are helpful to characterize the postbounce features in our 3D-GR model^{**)}. The top left panel shows the distribution of entropy per baryon at $t \approx 10$ ms, when the bounce shock stalls at a radius of ~ 90 km (shown as a central blueish sphere). Comparing the top left with top right panel in Fig. 7, we see that the shock (a greenish sphere in the top right panel) becomes bigger. This implies that the bounce shock turns into a so-called “passive” shock, which expands outward

*) Very recently, Müller et al.¹³⁷⁾ reported explosions for 11.2 and $15M_\odot$ stars based on their 2D GR simulations in CFC with detailed neutrino transport similar to 36) being implemented.¹³⁸⁾

***) The 3D computational domain is a cube of 10000^3 km³ volume fit in the Cartesian coordinates. The maximum refinement level in AMR is 5 at the beginning and then incremented as the collapse proceeds. The criterion for incrementation is renewed when the central density exceeds $10^{12,13,13.5}$ g/cm³, yielding an effective resolution of $\Delta x \sim 600$ m at bounce (see 140) for more details).

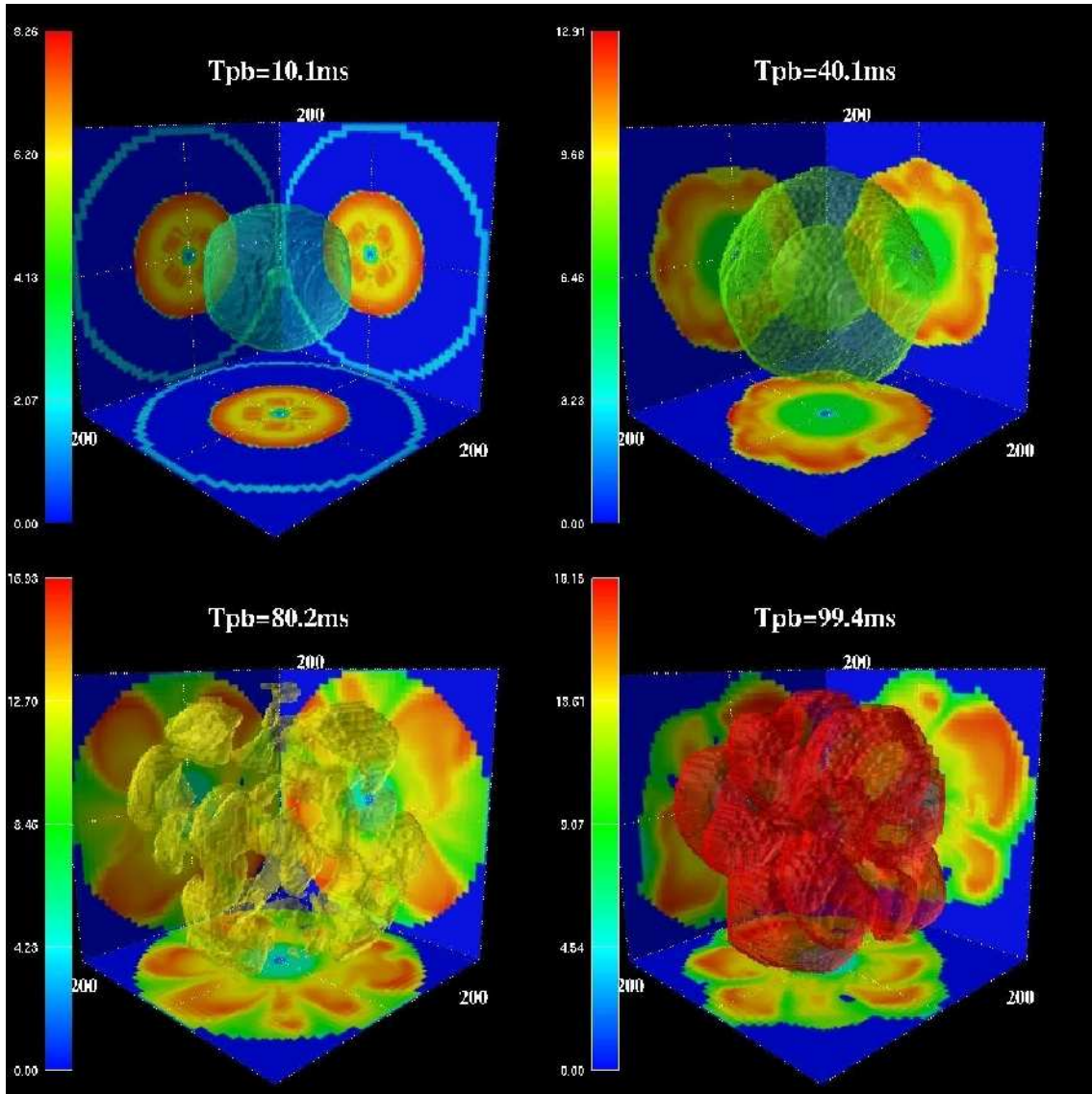


Fig. 7. 3D snapshots of entropy per baryon at four different times (top left; $t = 10\text{ms}$, top right; $t = 40\text{ms}$, bottom left; $t = 80\text{ms}$, and bottom right; $t = 100\text{ms}$) for model 3D-GR. The contours in the $x = 0$, $y = 0$, and $z = 0$ planes are projected on the back right, back bottom and back left sidewalls, respectively, to visualize the 3D structures. In each plot, an arbitrarily chosen iso-entropy surface is displayed. The linear scale is indicated along each axis in unit of km (figures taken from Ref.139), reproduced by permissions of the AAS).

gradually with all matter advecting inward after passing through the shock (e.g., 36)). At this stage, there forms a gain region, in which neutrino-heating dominates over local cooling. The neutrino-driven convection gradually develops from this point on. The sidewalls in the top right panel also demonstrate the growth of the postshock convection. The entropy behind the standing shock becomes higher with

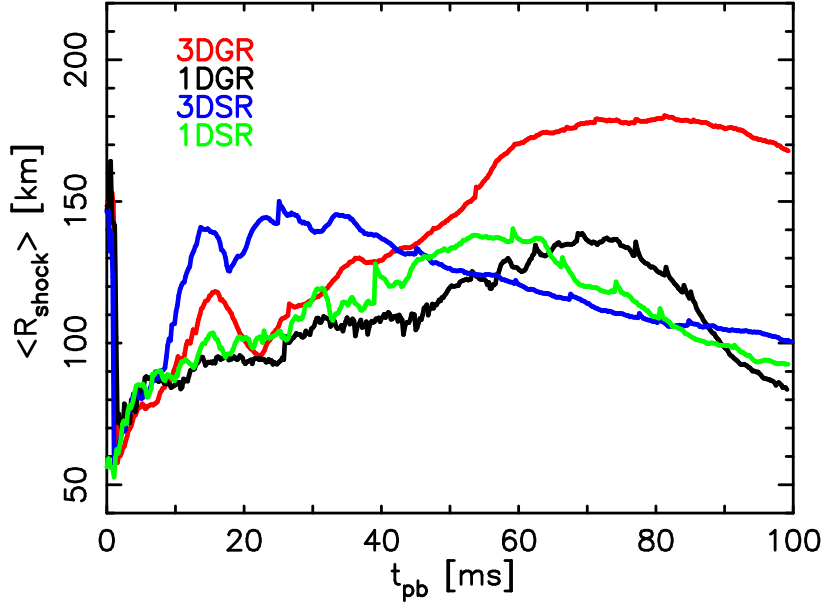


Fig. 8. Evolutions of average shock radii as a function of time after bounce for models 1D-SR (green line), 3D-SR(blue line), 1D-GR (black line), and 3D-GR (red line), respectively. The maximum shock radii and the time scale of shock recession for model 1D-GR is similar to those obtained in the previous 1D simulations for the same progenitor model that incorporated neutrino transport more in detail (e.g., 127,138).

time owing to the neutrino-heating, which can be inferred from yellowish bubbles in the bottom left panel. These high entropy bubbles ($s \gtrsim 10k_B$) rise and sink behind the standing shock. The shock deformation is dominated by unipolar and bipolar modes, which may be a characteristic feature of the SASI. The neutrino-heated region becomes larger with time in a non-axisymmetric way, which is evident in the bubbly structures that are shown as reddish regions in the bottom right panel.

In these simulations up to 100 ms after bounce, the largest shock radius is recorded in model 3D-GR (red line in Fig. 8). The other models have already seen the shock recession by this time. Before we focus on the reason for it in the next section, let us compare the activities of convection and SASI between the computations in SR and GR. Figure 9 displays the angle-averaged Brunt-Väisälä (BV) frequency ω_{BV} ³⁶⁾ (left panels) and pressure dispersion Δp^* in a logarithmic scale (right panels) for models 3D-SR (top two panels) and 3D-GR (middle two panels), respectively.

Irrespective of SR or GR, there are typically three convectively unstable regions in the postbounce phase: (1) the greenish region behind the shock^{**)} at $t \lesssim 20$ ms that corresponds to the so-called prompt convection, (2) a narrow horizontal strip behind the shock that corresponds to the convection sometimes referred to as Bethe convection, (3) a thick horizontal strip above the PNS at a radius of $r \sim 10 -$

*) This is defined as $\Delta p \equiv \frac{\sqrt{\langle p^2 \rangle - \langle p \rangle^2}}{\langle p \rangle}$, where $\langle A \rangle$ represents the angle average of quantity A .

***) Note that the shock is indicated by a white thin line that rises quickly after bounce and declines after the passive shock stalls at a radius of $r \sim 150$ km .

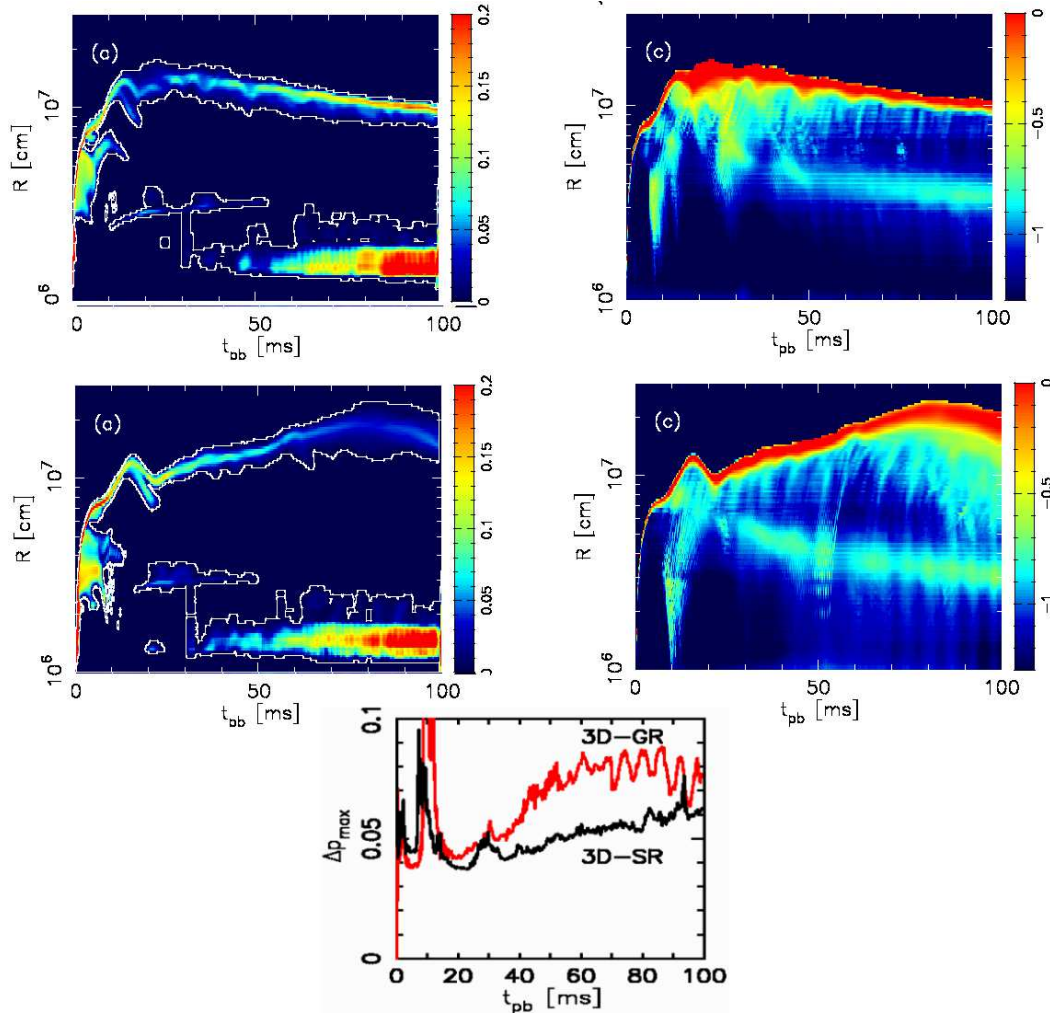


Fig. 9. Postbounce evolution of angle-averaged Brunt-Väisälä frequencies (ω_{BV} in ms^{-1}) (left panels) and pressure dispersions Δp (right panels) for models 3D-SR (top row) and 3D-GR (middle row), respectively, and the maximum pressure dispersion Δp_{max} (bottom row). Only convectively unstable regions (i.e. $\omega_{BV} > 0$) are shown and the white lines represent the boundaries of convective regions with $\omega_{BV} = 0$ in the left panels. In searching the maximum value of pressure dispersions for the bottom panel, we restrict the region to $20 \leq r \leq 50\text{km}$, i.e., the vicinity of the coupling radius (figures taken from,¹³⁹) reproduced by permissions of the AAS).

20km that emerges at $t \gtrsim 60\text{ms}$. Comparison between the two panels in the left column for models 3D-SR and 3D-GR shows that the unshocked core (the central part of PNS surrounded by the convective region) is more compact in the GR model at $t \gtrsim 50\text{ms}$. The PNS convection develops only very weakly before $t \sim 60\text{ms}$. This is common to both SR and GR cases and due to the stabilizing effect of a positive entropy gradient prevailing outside the PNS surface ($r \sim 10\text{km}$). The PNS convection becomes vigorous gradually with time afterward as the negative lepton gradient develops in the nascent PNS.

Next we pay attention to the right two panels of Fig. 9 to infer the activities of SASI. In these panels, we may recognize two horizontal strips: one is colored in red and shows strong pressure perturbations behind the shock; the other is colored in green and roughly corresponds to the bottom of cooling layer that recedes from $r \sim 80\text{km}$ to $r \sim 30\text{km}$ gradually in time from $t \sim 30\text{ms}$ to $t \sim 100\text{ms}$. The accreting flows that advect from the standing shock on to PNS receive abrupt decelerations near the bottom of the cooling layer. Strong pressure perturbations are produced there as mentioned above and propagate outward subsequently until they hit the shock. The up-going stripes in the figure seem to indicate these outward propagation of pressure waves. The features just mentioned may be reminiscent of the so-called advective-acoustic cycle (e.g., 145)–147) and references therein) and are common to the SR and GR models.

The bottom panel of Fig. 9 compares the maximum pressure dispersions that the advecting vortices produce in the vicinity of the deceleration region.^{*)} As is evident in the figure, the maximum pressure dispersion is generally larger in the GR model (red line) than the SR counterpart (black line) in the early postbounce phase ($t \lesssim 100\text{ms}$) we study here. This is presumably because stronger gravitation pull in GR makes the coupling radius smaller, leading to the production of more energetic acoustic waves. Although it is not straightforward to say something very solid only from this figure, what we observed so far in our 3D-GR model, i.e., the generation of stronger acoustic waves and larger shock radii in GR, suggests at least that 3D is not unfavorable for the neutrino-driven explosion. We now move on to more detailed discussions on potential impacts of 3D and GR on the neutrino-heating mechanism.

2.2.2. 3D versus GR: impacts on the neutrino-heating mechanism

Recalling that the neutrino heating rate can be expressed as $Q_\nu^+ \propto L_\nu \langle \epsilon_\nu^2 \rangle$,¹¹²⁾ we first analyze the neutrino luminosities (L_ν) and mean energies ($\langle \epsilon_\nu \rangle$). We then compare the dwell time with the neutrino-heating time in the gain region and discuss which one, 3D-SR or 3D-GR, is more likely to satisfy the criterion for shock revival.

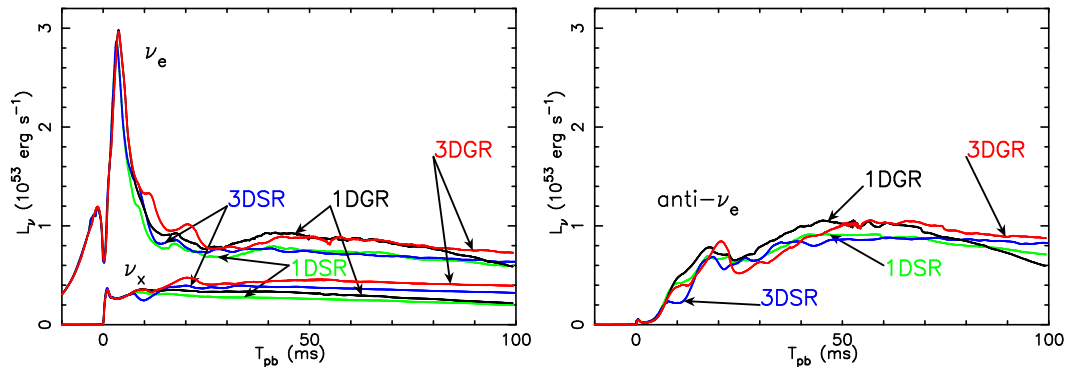


Fig. 10. Luminosities of all neutrino flavors for all the models as a function of time. ν_e and ν_μ are displayed in the left panel and $\bar{\nu}_e$ is presented in the right panel (figures taken from,¹³⁹⁾ reproduced by permissions of the AAS).

^{*)} Scheck et al.¹⁴⁷⁾ referred to this region as the "coupling radius", at which the coupling of vortices and acoustic waves takes place.

Figure 10 shows for all the computed models the evolutions of neutrino luminosities of all the species: ν_e , ν_x (left panel) and $\bar{\nu}_e$ (right panel). The spike in the ν_e luminosity is the so-called neutronization burst that occurs when the shock passes through the neutrino sphere for ν_e . The peak ν_e luminosities for the GR models are $L_{\nu_e} \sim 3 \times 10^{53} \text{erg s}^{-1}$, slightly larger than those for the SR models, ($L_{\nu_e} \sim 2.9 \times 10^{53} \text{erg s}^{-1}$) but are rather insensitive to dimensionality. This trend is qualitatively similar to what was found in 121). On the other hand, recent studies with weak interactions being treated in more detail in approximate Boltzmann transport have demonstrated that the peak ν_e luminosity is $\sim 10\%$ smaller in GR than in Newtonian gravity (e.g., 127), 138)). This may carry an important message that the Boltzmann transport should be implemented in the full GR simulations to obtain a $\sim 10\%$ accuracy, which is not small at all when speaking about the neutrino-heating mechanism.

After the neutronization burst ($t \gtrsim 10\text{ms}$), the ν_e luminosities increase with time in the GR models whereas they are almost constant in the SR models in the early postbounce phase up to $t \sim 100\text{ms}$ (green and blue lines in Fig. 10). The $\bar{\nu}_e$ luminosities are highest in model 3D-GR after $t \sim 50\text{ms}$ (red line in the right panel of Fig. 10). This is also the case for the ν_x luminosities (left panel). Although the luminosities change with time, the luminosities of different neutrino flavors satisfy the following orders in general:

$$\begin{aligned} \nu_e: & \text{ 3D-GR} > \text{1DGR}, \text{ 3D-SR} \sim \text{1D-SR}, \\ \bar{\nu}_e: & \text{ 3D-GR} > \text{1DGR}, \text{ 3D-SR} > \text{1D-SR}, \\ \nu_x: & \text{ 3D-GR} > \text{1DGR}, \text{ 3D-SR} > \text{1D-SR}. \end{aligned}$$

In short, both 3D and GR raise the neutrino luminosity in the early postbounce phase. More specifically, the maximal boost by GR, $\sim 50\%$, is obtained for ν_x in 3D as is found in the left panel of Fig. 10 whereas the maximum gain by 3D is less than $\sim 20\%$, which is obtained for $\bar{\nu}_e$ in the comparison between models 3D-GR and 1D-GR. These results indicate that GR holds a comparatively more important key to the neutrino luminosity.

The top two panels in Fig. 11 present the angle averaged RMS neutrino energies for ν_e (left panel) and $\bar{\nu}_e$ (right panel) after the neutronization burst ($t \gtrsim 10\text{ms}$). We obtain the highest energies in model 1D-GR (black line) and the second highest in model 1D-SR. Then comes model 3D-GR followed by model 3D-SR. In accord with the previous 1D results,^{121),127),138),148)} our 3D models (albeit limited to the early postbounce phase) support the expectation that we will obtain higher neutrino energies when switching from SR to GR. The deeper gravitational well in GR is the reason for the higher neutrino energies. In fact, PNS becomes more compact and, as a consequence, hotter in GR, which then leads to smaller and hotter neutrino spheres. This is evident when one compares the radii of neutrino spheres between the GR and SR models in the bottom panels of Fig. 11. Smaller neutrino energies in the 3D models compared with the corresponding 1D counter parts (top panels) are due to larger neutrino spheres in the former (bottom panels). In fact, the shock reaches larger radii in 3D, assisted by the convection and SASI (e.g., Fig. 8), which also helps shift the positions of neutrino spheres outwards. The enlarged neutrino spheres in multi-D models are qualitatively consistent with the 2D post-Newtonian

results by 36), which incorporated the advanced neutrino transport.

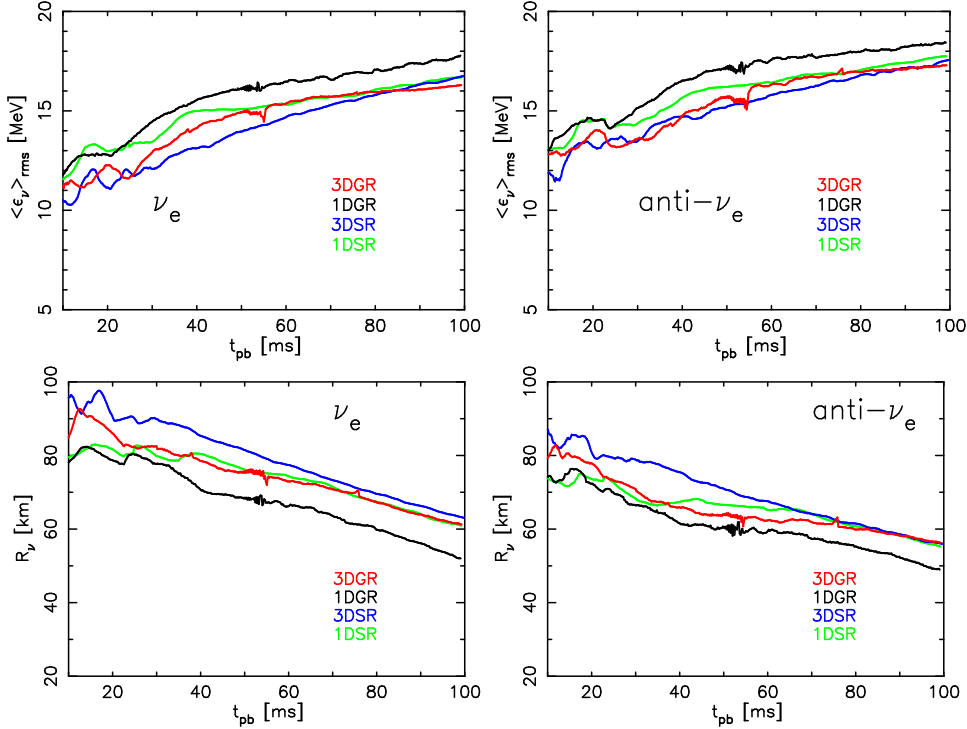


Fig. 11. Evolutions of the angle averaged RMS energies (upper panels) and the radii of neutrino spheres (lower panels) for ν_e (left panels) and $\bar{\nu}_e$ (right panels). The colors of lines are the same as those in Fig. 10 (figures taken from,¹³⁹) reproduced by permissions of the AAS).

Not all GR effects are good for the neutrino-heating mechanism. In fact, stronger gravitational pull in GR tends to shorten the residency times of accreting matter in the gain region. In the following we discuss whether the net GR effect, after all these effects being taken into account, is positive or not in the multi-D context. Figure 12 shows the ratio of the residency time scale to the neutrino-heating time scale for all the computed models. Although the computed time $\sim 100\text{ms}$ is way too short for the stalled shock to be revived, our results clearly suggest that the shock revival is most likely to occur in model 3D-GR (red line). Models 3D-SR, 1D-SR and 1D-GR follow it in this order. Thanks to larger degrees of freedom, the residency time scale is much longer in the 3D models than in the 1D models. In addition, the increases in neutrino luminosity and RMS energy via the GR effects (Fig. 11) raise the time scale ratio by a factor of $\lesssim 2$ in model 3D-GR (red line) from the SR counter part (blue line). Our results hence suggest that the combination of 3D and GR will provide the most favorable condition for the neutrino-driven explosion.

It is expected from Fig. 12 that the shock revival will never occur in the 1D models, which have already shown the sign of a rapid shock recession by the end of the simulations. On the other hand, the time scale ratio remains high in the 3D models for the last $\sim 30\text{ms}$ before the simulations are terminated. For the $15 M_\odot$ progenitor employed in this study, it is expected that the neutrino-driven

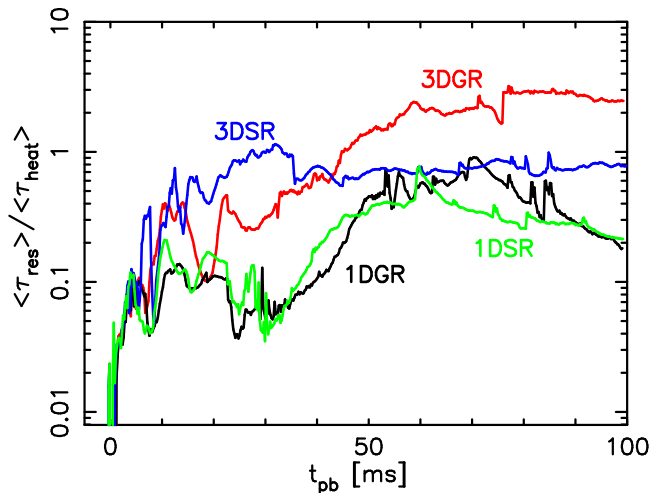


Fig. 12. The ratio of the residency timescale to the heating timescale for the set of our models as functions of post-bounce time (see text for the definition of the timescales). This figure is taken from,¹³⁹⁾ reproduced by permissions of the AAS.

explosions take place at $t \sim 200\text{ms}$ at the earliest⁴⁰⁾ and that it might be delayed to $t \gtrsim 600\text{ms}$ ³⁹⁾ as already mentioned. The parametric explosion models showed that the earlier the shock revival occurs, the stronger the explosion becomes^{44),56)}. The shock revival times obtained in the previous 2D simulations^{39),40),42),52)} could have been shorter if the combination of GR and 3D had been included. We anticipate that this can be a possible remedy to turn the relatively under-powered 2D explosions into more powerful ones. It is worth pointing out that the combination of GR and 3D*) should affect not only the supernova dynamics, but also the observational multi-messenger signatures (e.g., Ref. 74) for a recent review), such as gravitational-waves (e.g., 107),108),149)–151)), neutrino emission (e.g., 152)–154)), and nucleosynthetic yields (e.g., 155),156)). To give reliable predictions to these important observables, the multi-energy and multi-angle neutrino transport should be incorporated in full GR simulations together with more detailed weak interactions. This work is only a very first step on the long and winding road.

§3. Progresses in Boltzmann neutrino transport

3.1. Numerical simulations with Boltzmann equations: overview

We briefly overview here the recent progresses in the numerical treatment of neutrino transfer with exact Boltzmann equations in the CCSN simulations.^{157),158)} Although 3D computations of hydrodynamics are now made practicable thanks to large computing resources available these days, the neutrino transport in three spatial dimensions is still a great challenge. It is required to solve the time evolution of neutrino distributions in the six dimensional phase space with three components of

*) It should be mentioned that MHD effects also remain to be studied (e.g., 63),64),69)–73),140) and see also 2) for collective references).

neutrino momentum (an energy and two angles) in addition to three spacial dimensions. Even in spherical (axial) symmetry, three (five) dimensional computations are needed. Although various approximations have been proposed so far, solving exact Boltzmann equations is highly recommended so that we could remove uncertainties in the neutrino transfer, the key ingredient in the neutrino-heating mechanism. Simplifications such as just dropping energy or angle dependence are not reliable in principle, since neutrino interactions are strongly energy-dependent and angular distributions are essentially important to accurately estimate neutrino-heating rates in the semi-transparent region.

Under spherical symmetry, the direct solution of the Boltzmann equations for neutrino transfer is now possible^{(11), (13), (159), (160)} even in GR^{(14), (48), (148), (161)} with current computing resources. In fact, with these first-principle-based codes, the influences of EOS and various neutrino reactions on the supernova dynamics have been examined in detail over the years.^{(14), (36), (162), (163)} As mentioned already, it has been consistently demonstrated that no explosion is obtained under spherical symmetry. It is well established through the improvements in the numerical treatment of neutrino transport during these years, however, that the accurate computation of neutrino transfer is indispensable to determine the luminosity and energy spectrum of neutrinos emitted from the PNS and the heating rates behind the stalled shock, which will in turn affect the shock revival.^{(25), (126)} The Boltzmann neutrino transport is indispensable also for a reliable theoretical prediction of neutrinos signals,^{(13), (14), (97), (164), (165)} which should be compared with future observations by terrestrial neutrino detectors.^{(95), (166)–(168)}

With an assumption of axisymmetry, very elaborate, state-of-the-art, approximations have been developed in the last couple of years. The flux limited diffusion (FLD) method^{(58), (169), (170)} and the "ray-by-ray" extension of the 1D Boltzmann transport scheme^{(36), (39)} have been extensively employed to investigate multi-D effects on the explosion mechanism. Each approximation has its pros and cons: in the flux-limited diffusion approximation, for example, the transport in the semi-transparent region is not very reliable; in the "ray-by-ray" approximation, on the other hand, the neutrino transfer equations are solved along each radial ray independently and, as a consequence, although the computations are highly efficient, the forward-peaked distributions of neutrinos in the transparent region tend to be overestimated. Some of more recent works combine approximate 1D transport schemes such as FLD or IDSA with the ray-by-ray technique.^{(40)–(42)} These 2D simulations have demonstrated the critical role of hydrodynamical instabilities such as convections and SASI in the neutrino-heating mechanism. It should be also mentioned that the exact Boltzmann equations were also solved in 2D by^{(172), (173)} with the discrete-ordinate method, albeit for a limited number of models.

Spatially 3D simulations of core-collapse are still in its infancy. In most of the earliest 3D simulations^{(27), (29), (32), (174)} the neutrino transfer were just neglected or simplified considerably and the authors paid attention to novel features of 3D hydrodynamics, in particular instabilities such as convections and SASI. In the so-called light bulb approximation, for example, the neutrino luminosity and energy spectrum are not solved but prescribed parametrically to seek favorable conditions for shock revival.^{(56), (104)} More recently, by combining the ray-by-ray approximation

with FLD⁴⁰⁾ or IDSA,^{41),42),110)} 3D hydrodynamical simulations with spectral neutrino transport were performed.¹¹⁰⁾ These 3D computations heralded a new stage of supernova simulations. As already mentioned in section 2.1, these models did not have sufficient resolution yet and further improvements are needed. In this section we will make an attempt to go beyond such approximate neutrino transport schemes and solve the exact Boltzmann equations in 3 spatial dimensions, i.e., in 6D phase space. For the moment, relativity is neglected in the multi-D Boltzmann transport.

But before going to the multi-D transport, we will first summarize briefly our 1D GR radiation-hydrodynamical core-collapse simulations with a Boltzmann solver to demonstrate what insights can be obtained into microphysics with these simulations. We then report our recent progresses in the coding of multi-D Boltzmann solver, presenting the results of some test calculations.

3.2. 1D GR neutrino-radiation hydrodynamics with a Boltzmann solver

The first-principle simulations by solving the GR hydrodynamical equations and exact Boltzmann equations for neutrinos under spherical symmetry enable us to avoid uncertainties in numerics and investigate physics, in particular, the influences of microphysics on the dynamics in a quantitative manner (see also more recent works^{82),127),175)}). This is indeed a good example to see the close connections between the latest knowledge on nuclear/particle physics in laboratory and the understanding of astrophysical phenomena. We discuss here how EOS at high densities impacts the postbounce dynamics and what information on EOS can be extracted from them in return. In the following, we summarize our 1D results for $15M_{\odot}$ and $40M_{\odot}$ stars, paying particular attention to the light curve and energy spectrum of neutrinos obtained in the long-term postbounce evolution.^{14),94),96),164),176)–178)}

3.2.1. Competing effects of nuclear EOS on the core dynamics

In the case of the $15M_{\odot}$ star, we computed the evolution up to ~ 1 s after bounce¹⁴⁾ to find out the fate of the stalled shock and see the thermal evolution of PNS (see also the long term evolutions by 165)). We adopt two EOS's as in the previous sections, i.e., Shen's EOS^{87)–89)} and Lattimer& Swesty's EOS with an incompressibility of 180MeV.⁴⁵⁾ We found that neither EOS produced explosions and that the shock radii are rather similar in the two cases despite the different features of the EOS's (Shen's EOS is harder than Lattimer & Swesty's). It turns out that a number of effects are counteracting each other.

On one hand, the larger symmetry energy of Shen's EOS leads to a smaller abundance of free protons, which then reduces electron captures¹⁷⁹⁾ and make the inner core at bounce more massive, as can be seen in Fig. 13. Note that a larger inner core is favorable for explosion. The difference in core mass amounts to $\sim 0.1M_{\odot}$, which can sap the shock energy of $\sim 10^{51}$ erg by dissociation of heavy nuclei. On the other hand, stiffer Shen's EOS produces core bounce at a slightly lower density and, as a consequence, gives a lower core temperature than Lattimer & Swesty's. This then reduces the neutrino luminosity and leads to lower heating rates behind the shock as demonstrated in Fig. 13. This way the advantage earned during the collapsing phase is almost canceled out in the post-bounce phase. Note that the

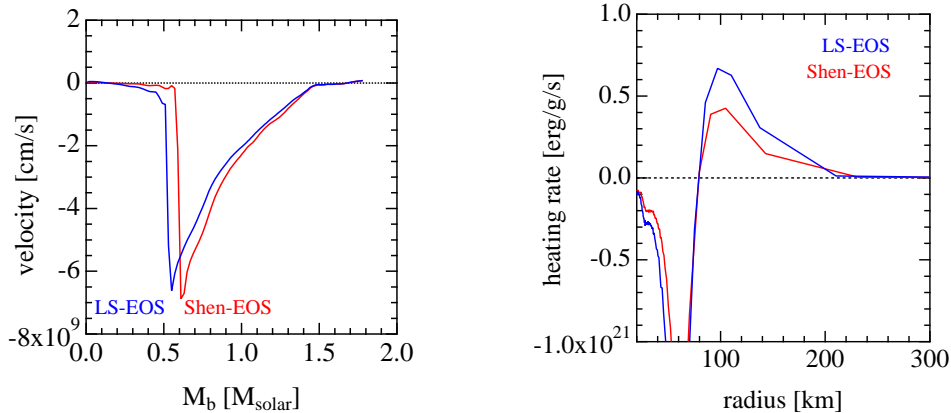


Fig. 13. The velocities at core bounce (left) and heating rates at $t = 150$ ms after bounce (right) in the collapse of $15M_{\odot}$ star. The red and blue lines show the results obtained with Shen’s and Lattimer & Swesty’s EOS’s, respectively.

electron captures on nuclei may dominate over those on free protons.¹⁶²⁾ In order to address this issue appropriately, we need to implement a multi-nuclei EOS at sub-nuclear densities.^{90),91),99),180)} Note that the standard EOS’s (including Shen and Lattimer & Swesty) employ the so-called single nucleus approximation, in which an ensemble of heavy nuclei is represented by a single, supposedly most abundant nucleus. Note again that the most abundant nucleus need not have the largest electron capture rates. In fact, one has to take an ensemble average of the electron capture rate multiplied by the abundance of individual nucleus. It is also stressed that microphysics such as EOS and weak interaction rates is important also in multi-D simulations, since they set the initial shock energy and the emission and absorption of neutrinos just in the same way we have seen above.

3.2.2. Neutrino signals from failed supernovae: extraction of information on EOS

The long-term simulations of core-collapse of the $40M_{\odot}$ star provides us with an opportunity to study black formations and neutrino signals from them. In fact, since the size of Fe core is much larger compared with that for $15M_{\odot}$ star, it is expected that there is no chance of explosion and that continued mass accretion from outer envelopes will eventually cause the second collapse to black hole.^{181)–183)} Indeed the mass of PNS increases rapidly and it reaches the critical mass in ~ 1 s and triggers the dynamical collapse to the black hole.^{96),97),148)} During the thermal evolution of the central object, the neutrinos are copiously emitted by electron and positron captures as well as thermal productions. The neutrino emission is terminated soon after the event horizon is formed and the emission region is swallowed into it. Hence the duration of the neutrino emission is essentially determined by the time of the second collapse of the accreting PNS into the black hole.

In order to specify common and different characters of hydrodynamics and neutrino emission in the black-hole forming collapse, we investigated other progenitor models in the mass range of $40–50M_{\odot}$.^{96),164),176)} In addition to the standard EOS’s,

we also employed hyperonic EOS^{177),178)} as well as quark EOS.⁹⁴⁾ In Fig. 14 we show the comparison of the three EOS's: Shen's EOS, Lattimer & Swesty's EOS (with an incompressibility of 180MeV) and hyperonic EOS. It is evident that the energies and luminosities of neutrinos rise rapidly due to the increase of temperatures inside the slowly contracting PNS and the persistent mass accretion. The duration of the neutrino emission is only 0.6-1.3 s. These features are different from those for the ordinary neutrino emission in supernovae, which last ~ 20 s with gradually decreasing energies and luminosities. Hence, it is possible to distinguish the black hole formations from the neutron star formations by the neutrino signals. In fact, taking properly into account the detector properties as well as neutrino oscillations, we estimate that Super-Kamiokande will record $\sim 10^4$ events for a galactic event,^{95),168)} which are comparable to those for ordinary supernovae.¹⁸⁴⁾

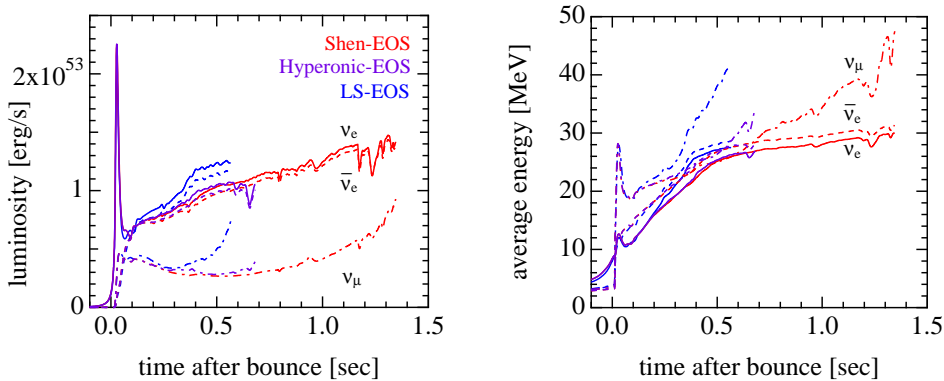


Fig. 14. Time profiles of the neutrino emission in the collapse of the $40M_{\odot}$ star. The neutrino luminosities (left) and average energies (right) of three neutrino species are shown for three EOS's: Shen's EOS, Lattimer & Swesty's EOS and Hyperonic EOS.

As is evident in Fig. 14, the features of neutrino emission in the black-hole forming collapse are sensitive to EOS at supernuclear densities. A softer EOS ends up with shorter neutrino emission, since the critical mass for the second collapse to black hole is lower.^{96),164)} The reason for the softening of EOS may be due to interactions between baryons or to the emergence of new degrees of freedom such as hyperons^{177),178)} or quarks.⁹⁴⁾ We further analyzed the neutrino signals obtained with the rather soft nucleonic EOS (Lattimer & Swesty's EOS with an incompressibility of 220MeV) and with the Hyperonic EOS⁹⁵⁾ by a statistical method. We demonstrated that although the durations of neutrino emission are similar to each other, they are still distinguishable by Super-Kamiokande if they occur in the Galaxy. These differences of signals in turn can be used as a useful probe into the EOS at very high densities, which may be accessible to the next-generation terrestrial experiments.^{95),168)} It should be mentioned that the features of dynamics and neutrino emission depend also on the profile of progenitors mainly through the accretion rate.^{97),176)} Hence, it is important to perform more systematic simulations and construct the templates of signals that can be compared with future observations.^{167),168),185),186)}

3.2.3. Parallel computing in 1D simulations

It is profitable to comment on the aspect of supercomputing in the 1D studies. In our numerical simulations described above, the numerical inversion of block tridiagonal matrices that appear in the discretization and linearization of basic equations is the major computational load. We implemented the block cyclic reduction¹⁸⁷⁾ as an efficient parallelised algorithm of matrix inversion that replaces the conventional, serial algorithm of the Feautrier method.¹⁸⁸⁾ The numerical technique developed for 1D spherically symmetric neutrino transfer can be easily extended to multi-D by the use of the approximate ray-by-ray implementation of Boltzmann solvers.

3.3. *Multi-D neutrino transport: numerical solutions of 6D Boltzmann equations*

Thanks to recent expansions of supercomputing resources, it has now become feasible to numerically solve the Boltzmann equations for neutrino transfer in three spacial dimensions. We have indeed developed a Boltzmann solver with multi-energy and multi-angle groups that is meant for multi-D simulations.¹⁵⁸⁾ The code is based on the so-called discrete-ordinate (S_n) method in six dimensions (see Ref. 189) for an alternative approach by Monte Carlo scheme).

We describe the neutrino distribution in the space coordinate with radial N_r -, polar N_θ -, and azimuthal N_ϕ -grid points and in the neutrino momentum space with energy N_ϵ -grid points and angle N_{θ_ν} - and N_{ϕ_ν} -grid points. A fully implicit differencing is adopted for time advancement. We choose the inertial frame to write down the Boltzmann equations, in which the advection terms have the simplest expressions. Then we need to consider the Lorentz transformations to evaluate the collision terms, which become simplest in the comoving frame. For the moment, however, neglecting all the corrections of the order of v/c or higher, we do not distinguish these two frames*).

The basic set of neutrino reactions^{14),122)} including pair processes but not inelastic scatterings is implemented in the collision terms. Three species of neutrinos ($\nu_e, \bar{\nu}_e, \nu_{\mu/\tau}$) are treated. The standard EOS tables are employed to obtain the thermodynamical quantities and composition of matter, which are necessary to evaluate the collision terms. In the following test computations we adopt Shen's or Lattimer & Swesty's EOS.

3.3.1. Some basic tests

A suit of numerical tests have been done to validate the newly developed Boltzmann solver. We have first computed multi-D transport in uniform matter both in the diffusion and free streaming regimes. In the left panel of Fig. 15, the results of 2D/3D diffusion of Gaussian packets are displayed. We have found a satisfactory agreement with the exact solutions. In the right panel of the same figure, on the hand, we have shown the free propagation of neutrinos in a designated direction. Substantial numerical diffusion are apparent in this case. Note that this test is too demanding and no such situation becomes important in supernova simulations. The intermediate regime, the most important one, have been examined by utilizing the

*) We have an idea to rigorously treat the Doppler effects and angular aberrations in the collisional integrations and will publish it elsewhere

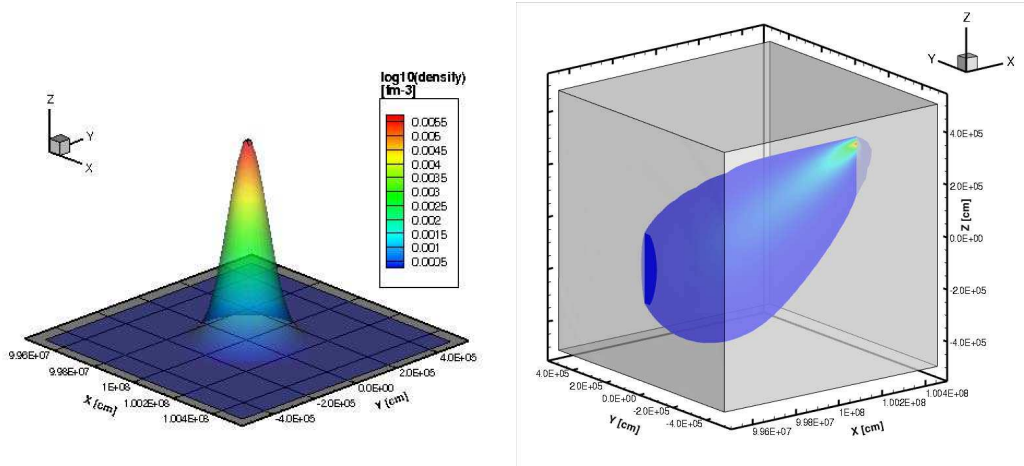


Fig. 15. Examples from the test suit of the time evolution of neutrino distributions by the 3D Boltzmann solver. Snapshot of neutrino density from the time evolution of the diffusion of 2D Gaussian packet by surface plot (left) and the neutrino beam from the point source in 3D box (right). The color expresses the neutrino density. The number of grid points is $N_r \times N_\theta = 100 \times 96$ (left) and $N_r \times N_\theta \times N_\phi = 50 \times 48 \times 48$ (left) with $N_{\theta_\nu} \times N_{\phi_\nu} \times N_\epsilon = 12 \times 12 \times 4$.

formal solutions for more realistic matter distributions as in the following.

We prepare artificially deformed spheroidal/ellipsoidal cores based on the post-bounce profile obtained in the 1D GR neutrino-radiation hydrodynamical core-collapse simulations of the $15M_\odot$ star.¹⁴⁾ With the background profiles of density, proton fraction and temperature being fixed, we follow the time evolution from a certain initial condition for a sufficiently long period (~ 10 ms) to obtain the steady neutrino distributions. In this computation we adopt the Shen's EOS table for the evaluation of the collision terms. The neutrino densities and fluxes are evaluated by appropriate integrations of the neutrino distribution functions over the momentum space. Various angle- and energy moments of the neutrino distribution functions including the flux factor and Eddington tensors are also examined (see 158) for detailed analyses). Moreover, we have also obtained from the collision terms the detailed information on neutrino reactions such as mean free paths, deleptonization rates and cooling/heating rates.

In Fig. 16, we show the results for the axially symmetric, spheroidal core. An oblate PNS sits at the center and the shock is standing around 140 – 200km in this model. The electron-type neutrinos (top left panel) and anti-neutrinos (top right panel) are abundant at and off center, respectively, reflecting the degeneracy of electrons. It is as expected intuitively for the oblate shape of the core that the radial flux is enhanced near the polar axis. The polar fluxes (θ -component of the flux vectors) are substantial at intermediate polar angles, since the neutrino fluxes are inclined towards the polar axis.

In Fig. 17, we show the 3D case, in which the core is deformed to a non-axisymmetric, ellipsoidal shape by adding an azimuthal (ϕ) dependence to the spheroidal configuration employed above. Displayed in the figure are densities and fluxes of

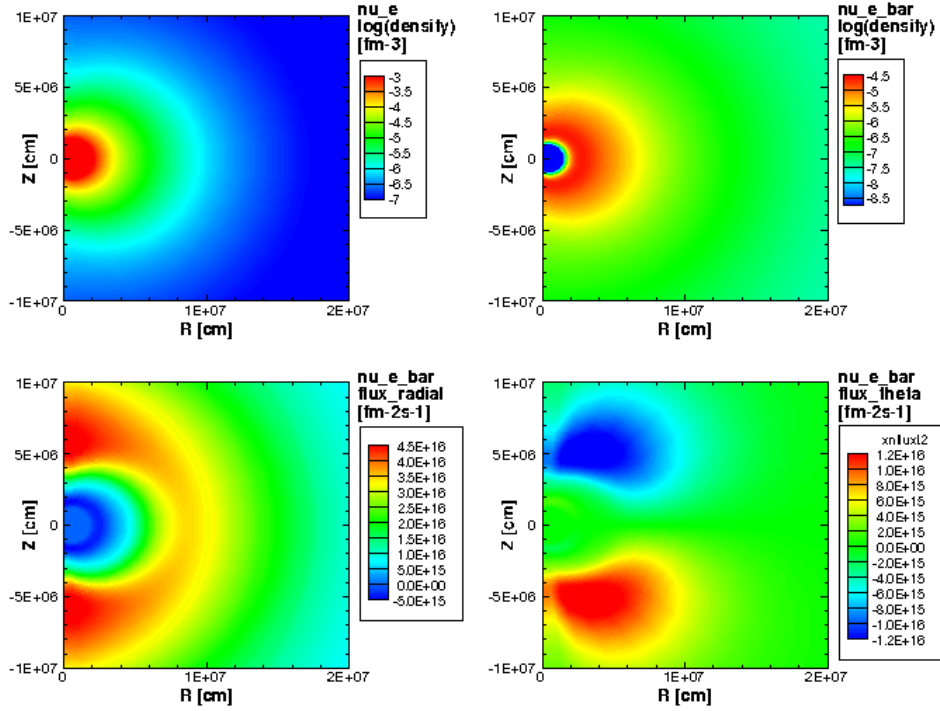


Fig. 16. Color maps of neutrino densities and fluxes in the half of meridional slice for an axisymmetrically deformed spheroidal core. The top panels display the densities of electron-type neutrinos (left panel) and anti-neutrinos (right panel) whereas the bottom left and right panels present the radial and polar components of flux vectors of electron-type anti-neutrinos, respectively. The number of grid points is $N_r \times N_\theta \times N_\phi = 200 \times 18 \times 9$ with $N_{\theta_\nu} \times N_{\phi_\nu} \times N_\epsilon = 6 \times 12 \times 14$.

three species of neutrinos in the first octant of a meridional slice with an azimuthal angle of $\phi = 0.44$ radian. The asymmetry between the pole and the equator in this slice is slightly smaller than that in Fig. 16. The density of electron-type neutrinos is high at center whereas electron-type anti-neutrinos and mu-type neutrinos are abundant off center, where the temperatures are higher than at center. This feature is similar to what we saw in the previous axisymmetric case. The fluxes of electron-type anti-neutrinos reflect the 3D deformation, though (lower panels of the figure). The radial flux around the polar axis is larger than that near the equatorial plane although the asymmetry is less remarkable compared with the 2D case. The polar fluxes are again non-negligible and largest at intermediate polar angles. Owing to the azimuthal dependence of deformation, the azimuthal fluxes are non-vanishing and substantial indeed in the broad region around $r = 50 - 100$ km. These non-radial fluxes are important to accurately describe the global behavior of neutrino transfer in 3D and may affect the neutrino heating rates and, as a consequence, explosions. We remark that these non-radial fluxes can be automatically and properly treated by the 3D Boltzmann solver unlike the ray-by-ray approximation, in which the neutrino fluxes are assumed to be radial. It is also pointed out that the non-radial fluxes are non-negligible up to ~ 100 km and it is dubious that FLD can give the flux vectors

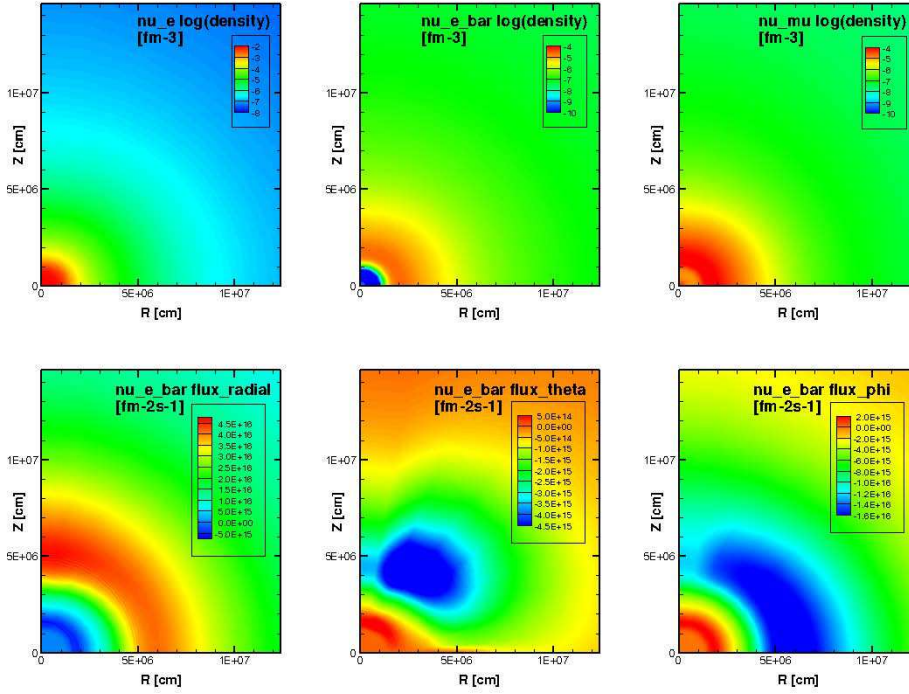


Fig. 17. Color maps of neutrino densities and fluxes in the quadrant of meridian slice for a non-axisymmetrically deformed ellipsoidal core. The densities of electron-type neutrinos (left panel), anti-neutrinos (middle panel) and mu-type neutrinos (right panel) are shown on the top rows whereas the radial (left panel), polar (middle panel) and azimuthal (right panel) components of the flux vectors of electron-type anti-neutrinos are shown, respectively, on the bottom row. The number of grid points is $N_r \times N_\theta \times N_\phi = 200 \times 9 \times 9$ with $N_{\theta_\nu} \times N_{\phi_\nu} \times N_\epsilon = 6 \times 12 \times 14$.

correctly there (see also Ref. 172)).

3.3.2. Several demonstrations for more realistic backgrounds

We proceed to some more test computations done under more realistic settings. We employ the snapshot at 100 ms after bounce that is obtained in the simulations of the $11.2M_\odot$ star¹¹⁰) discussed in §2. In the left panel of Fig. 18, we show the 3D entropy distribution in the supernova core. It is clear that the matter distribution is deformed both globally and locally due to the hydrodynamical instabilities below the shock (shown as a greenish sphere), which is located around 200–300 km. Adopting Lattimer & Swesty’s EOS for this test and fixing the background, we follow the time evolutions of neutrino distribution functions in the 6D phase space from an almost vanishing population until time-independent solutions are obtained. The Boltzmann solver treats the building up of equilibrium distributions in the optically thick region, neutrino cooling and heating in the intermediate region and outward free streaming in the optically thin outer layers simultaneously. A snapshot of some surfaces with a constant density of anti-neutrinos is shown in the right panel of Fig. 18. It is seen that the neutrino distribution is rather spherical near the center and becomes

asymmetric globally and locally in the outer layers, tracing the matter distributions (compare with the left panel).

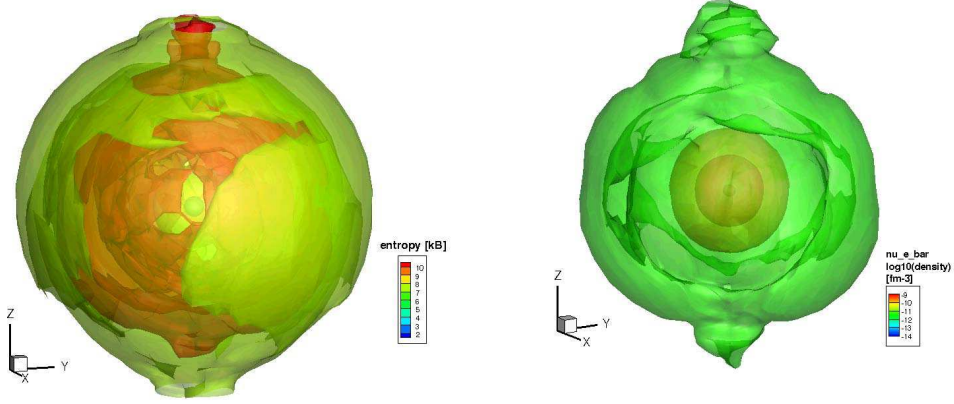


Fig. 18. Iso-entropy surfaces at 100 ms after bounce in the collapse of the $11.2M_{\odot}$ star (left panel) and surfaces of a constant density of electron-type anti-neutrinos in the evolution by the Boltzmann equations (right). The number of grid points is $N_r \times N_{\theta} \times N_{\phi} = 128 \times 16 \times 32$ with $N_{\theta_{\nu}} \times N_{\phi_{\nu}} \times N_{\varepsilon} = 6 \times 12 \times 14$.

Fig. 19 shows the computed density of electron-type anti-neutrinos (left panel) and net heating rates (right panel) on a slightly off center slice, respectively. The electron-type anti-neutrinos are abundant again in the off center region, where the temperature is high and all flavors of neutrinos are produced thermally. The isodensity surfaces are prolate, reflecting the matter distributions. The gain radius is located around $r \sim 100$ km and the global asymmetry of heating/cooling regions is moderate. The heating/cooling rates are calculated directly from the integrations of the collision terms. For implementing the radiation module in a hydrodynamic code, these quantities describing the changes in energy and compositions of matter enter in the right-hand-side of the hydrodynamic equations (with negative sign). This is what we are currently undertaking (Nagakura et al. in preparation¹⁹⁰). And then, the next important task is to implement the velocity dependent terms in the transport equations, which is indispensable for the accurate treatment of the relativistic effects. After that, we plan to study hydrodynamical instabilities in the supernova core, then move on to perform a full-scale simulation starting from the onset of gravitational collapse, through core bounce to shock-stall, until shock revival and explosion in a consistent manner. In doing so, highly competitive supercomputing resources in Japan, in particular the “K computer”^{*}, the fastest one in the world as of November 2011, will be helpful.

^{*}) it is named after the Japanese word of “Kei”, meaning 10 quadrillion (10 petaflops). Note that the given name of the corresponding author of this paper has nothing to do with the supercomputer (except for the fact that the person is going to use it for SN simulations).

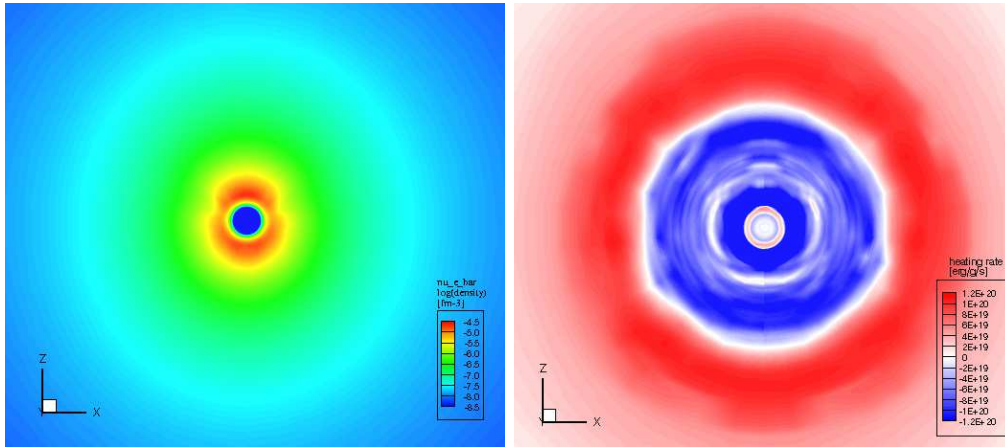


Fig. 19. The density of electron-type anti-neutrinos (left) and net heating rate (right) at 100 ms after bounce on a slightly off-center slice. The background matter distribution is obtained from the 3D simulation of $11.2M_{\odot}$ progenitor and fixed in the computations of neutrino transport.

3.3.3. Neutrino transport in highly non-spherical environments: collapsars

As an additional demonstration of the capability of our new 3D code, we take the collapsar model for gamma ray bursts,^{191),192)} which are more energetic and asymmetric than CCSNe. Gravitational collapse of very rapidly rotating, massive cores results in the formation of black hole with a surrounding disk, which is presumably responsible for jet formations. To pin down the physical processes to form the relativistic jets in the collapsar model is a long-standing issue. Annihilations of neutrino pairs emitted from the disks are one of the plausible mechanisms (e.g.,^{193)–196)} and references therein). Mass ejections from the disk and/or jet through neutrino interactions are attracting broad attention in the studies of nucleosynthesis of heavy elements.^{197)–200)} Neutrino transport in the collapsar model is hence an indispensable ingredient for the investigations both of jet formations and nucleosynthesis. Since the black hole and disk system is highly non-spherical, numerical approaches are almost mandatory. Although extensive studies mainly by utilizing a ray-tracing technique have been reported so far to this end,^{201)–205)} the spectral treatment of neutrino transfer has been a major undertaking. As a very first step toward better description of neutrino transport in collapsar, we employ our 3D code here to obtain time-independent neutrino distributions (see also Ref. 206)) for a matter configuration extracted from a hydrodynamical simulation of collapsar.

Distributions of density, temperature and electron fraction are provided by 2D GR simulations of gravitational collapse of a $100M_{\odot}$ star with a rapid rotation.^{144),207)} The density profile after black hole formation is shown in the left panel of Fig. 20. The black hole sits at the center, which is removed in the neutrino calculation and shown as a white circle in the figure, and a dense disk surrounds it. Not shown explicitly in the figure, there are accretions and outflows outside the disk. Fixing the matter distribution, we compute the time evolutions of neutrino distribution functions until the steady state is reached. We adopt the Shen’s EOS table

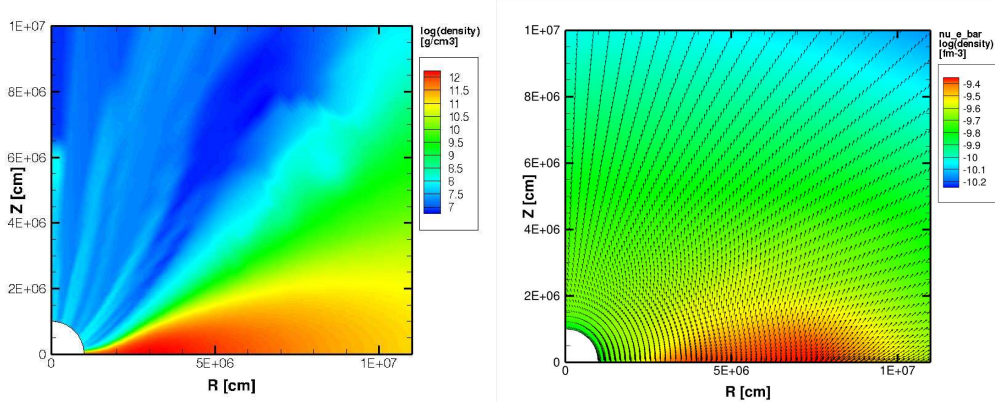


Fig. 20. The density profile in the quadrant of a meridian section used for the computation of neutrino transport with the Boltzmann solver (left) and the resultant steady distributions of electron-type anti-neutrinos (right). The neutrino densities are shown by a color map in log scale and fluxes are presented by arrows in the right panel. The number of grid points is $N_r \times N_\theta \times N_\phi = 100 \times 45 \times 3$ with $N_{\theta_\nu} \times N_{\phi_\nu} \times N_\varepsilon = 6 \times 12 \times 14$.

for this simulation.

The density of electron-type anti-neutrinos is shown in the right panel of Fig. 20. It is found that the electron-type anti-neutrinos are abundant in the outer part of the disk, where the temperatures are high, whereas the density of electron-type neutrinos (not shown in the figure) is high near the the black hole. The neutrino fluxes (shown as arrows in the figure) reflect the geometry of the system, very roughly agreeing with the local gradient of neutrino density, and completely non-radial. This is a situation that the ray-by-ray approach is certainly inappropriate. Detailed information such as the location of neutrino spheres and energy spectra of all species of neutrinos is essential to investigate the dynamics of outflows and nucleosynthesis inside them. We will address these issues in the near future with the new Boltzmann solver, which will be combined with a 3D GR hydrodynamics code described in section 2.2.

3.3.4. Progresses in the new algorithms for large-matrix inversion

It is worth mentioning that the exact 3D Boltzmann solver demonstrated above is a product of our collaboration with computational scientists, who know how to make best use of computing resources. They are specialists indeed in the mathematical modeling, algorithms and parallel computing. In this section, we briefly describe our recent progresses in this aspect of the development of the 3D Boltzmann solver.

As mentioned earlier, our scheme is based on the finite differencing of the Boltzmann equations (S_n method), which is implicit in time. The resulting equations are a linear system with a large sparse matrix. The main computational load comes from the inversion of this matrix, which has to be done at every time step. In the left panel of Fig. 21, we show the positions of non-zero elements in the matrix we obtain from the discretization of the original equations. It is found that the matrix consists of dense sub-matrices along the diagonal line (shown as gray boxes in the figure) as well as non-zero elements on six off-diagonal lines (labeled as x_1 , x_2 and x_3 in the

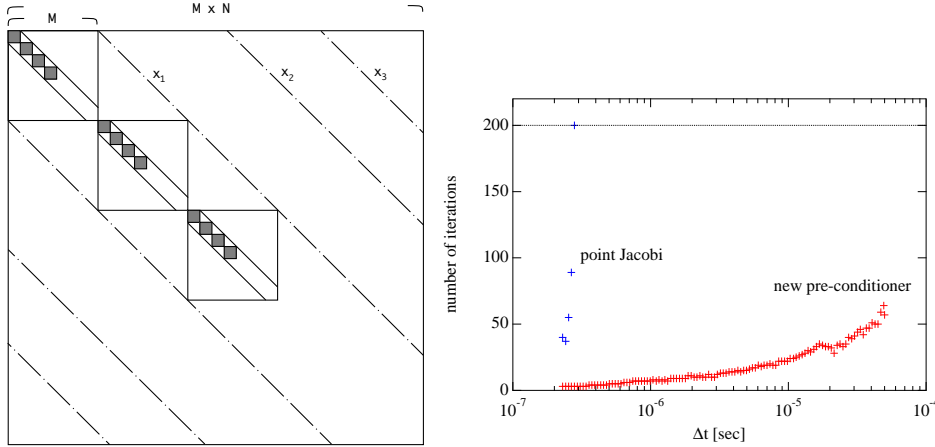


Fig. 21. Left: pattern of the sparse matrix appearing in the linear system obtained for the implicit discretization of the Boltzmann equations. N and M denote the numbers of spatial grids ($N_r N_\theta N_\phi$) and neutrino grids ($N_{\theta_\nu} N_{\phi_\nu} N_\varepsilon$), respectively. For the studies on the current supercomputers without energy couplings, the size of diagonal black matrices (gray) is $N_{\theta_\nu} N_{\phi_\nu}$. Right: number of iterations as a function of the time step for different pre-conditioners, i.e., the point Jacobi method (blue crosses) and newly developed method (red crosses). The number of grid points for the numerical experiment is $N_r \times N_\theta \times N_\phi = 200 \times 9 \times 9$ with $N_{\theta_\nu} \times N_{\phi_\nu} \times N_\varepsilon = 6 \times 12 \times 14$.

figure). The sub-matrices originate from the collision terms that express local emission and absorption of neutrinos as well as coupling by neutrino scattering moving in different directions, whereas the off-diagonal lines of non-zero elements corresponds to the spatial advection terms. The total number of grid points in the 6D phase space amounts to $\sim 10^9$ in a typical simulation. The size of dense sub-matrix is ~ 100 in the current studies and will be larger for higher angular resolutions and/or full energy-couplings.

For the inversion of matrices of this size, iterative methods²⁰⁸⁾ are the first choice. We employ as a standard option the Bi-CGSTAB method, utilizing a program in the Templates library,²⁰⁹⁾ together with the point-Jacobi method as a pre-conditioner. We obtain convergence typically within 20 iterations with a residual error of 10^{-8} . This is of course a function of the time step, Δt . As we increase it, convergence becomes slower because the diagonal elements become less dominant. As a matter of fact, sometimes no convergence is obtained even after 200 iterations in the simulations for realistic matter distributions extracted from dynamical models in §3.3.2. We certainly need to find a better way to improve convergence.

Recently we have found a new method to optimize the pre-conditioning. Taking out a set of the matrices from our simulations of 3D neutrino transfer, which presents the slow-convergence problem in the standard approach with the point-Jacobi method, their properties have been analyzed in detail to propose a parameter-optimized damped Jacobi-type pre-conditioner, details of which will be published elsewhere.²¹⁰⁾ The convergence efficiency is compared between the two pre-conditioners for the same matrices extracted from the 3D Boltzmann simulations. In the right panel of Fig. 21, we show the numbers of iteration as a function of the time step, Δt ,

for a representative case. As mentioned already, the convergence becomes very slow for $\Delta t \gtrsim 10^{-7}$ s and no convergence is obtained for $\Delta t > 3 \times 10^{-7}$ s even after 200 iterations when the point-Jacobi method is employed. On the contrary, with the new pre-conditioning method, the convergence is improved drastically. The time steps can be increased by a factor of 100 up to $\gtrsim 10^{-5}$ s. This is favorable particularly for long-term computations. It is true that the computational cost of the new method is higher but it is just by a factor of ~ 10 compared with the standard method. Our efforts have hence paid off and we have achieved a speed-up by a factor of ~ 10 . We are currently applying the new method to various cases to see if such a good performance is retained or not. We will also continue to seek for even better methods, since we expect that the matrix will be larger in the productive runs of neutrino-radiation hydrodynamical simulations in 3D.

§4. Beyond the “K computer”

Rapid growth of the supercomputing capability in Japan these years enables us to perform large-scale simulations such as those presented above. 3D supernova simulations with sufficient resolutions definitely require the K computer and more even beyond Exa-flops scale platforms. We remark also that allocations of sufficiently long cpu-time on such facilities are also indispensable for long-term computations such as those of delayed neutrino-driven explosions.

As reported in §2 and §3.3.2, the first 3D simulations of core-collapse supernovae with spectral neutrino transport by the ray-by-ray IDSA were performed on the currently available supercomputers. It was demonstrated that the numerical grid deployed in the computations was not fine enough to draw a solid conclusion on the 3D explosion mechanism. Scaled-up simulations are scheduled on the K computer in Kobe, Japan. The 3D neutrino transfer with the Boltzmann solver requires even larger memory and speed specifications. Summarized in Table I are the target sizes of numerical grids we deploy for the 3D Boltzmann transport as well as the required memory sizes and expected operation numbers per time-step on both the current and future platforms. Note that we have to follow more than 10^5 time-steps for a productive run.

We assume in the table that the computational load mainly comes from the inversion of the sub-matrices that account for the local emission and absorption as well as scattering of neutrinos; the operation numbers for the currently adopted inversion scheme, i.e., the Bi-CGSTAB method with the preconditioner discussed above, are proportional to $N_\epsilon N_{angle}^3$, in which N_ϵ and N_{angle} are the number of energy and angle grid points for neutrino transport, respectively; the latter gives the size of the dense sub-matrices on the diagonal line, since the scatterings couple different angular grid points. It is found that on the currently available supercomputers, we can afford only moderate resolutions for the 3D transfer, limited by the necessary memory size, which amounts to 2TB for the storage of the sparse matrices in the linear system (plus 20GB for the distribution functions of three species of neutrinos). The number of floating-point operations per time-step is estimated to be 6×10^{12} for a single species of neutrinos.

Table I. Target grid sizes and required computational resources for the current and future supercomputers. The currently available (typical) supercomputers, the K computer, Exa-scale supercomputers and beyond are listed. The numbers of radial, polar and azimuthal grid points in the space (N_r, N_θ, N_ϕ) and those of angles and energy grid points in the momentum space ($N_{\theta_\nu}, N_{\phi_\nu}, N_\epsilon$) are given together with the required memory sizes for the storage of the distribution functions of 3 species of neutrinos (4th column denoted as f_ν 's) and the matrix in the system of linear equations (5th column denoted as Matrix) as well as the floating-point operations (6th column denoted as Operations). The last row refers to the case, in which energy couplings by inelastic scatterings are fully taken into account.

Platforms	Space ($N_r N_\theta N_\phi$)	Neutrino ($N_{\theta_\nu} N_{\phi_\nu} N_\epsilon$)	f_ν 's	Matrix	Operations
Current	$256 \times 32 \times 64$	$8 \times 12 \times 14$	2×10^1 GB	2 TB	6×10^{12}
K computer	$512 \times 64 \times 128$	$12 \times 24 \times 20$	6×10^2 GB	2×10^2 TB	2×10^{15}
Exa-scale	$512 \times 128 \times 256$	$24 \times 24 \times 24$	6 TB	3 PB	8×10^{16}
E_ν -coupling	$512 \times 128 \times 256$	$24 \times 24 \times 24$	6 TB	8×10^1 PB	4×10^{19}

With the K computer, which is now in operation, we can deploy twice finer spatial, energy and angle grids; the memory size is 2×10^2 TB for the storage of matrices and 6×10^2 GB for the neutrino distribution functions; the floating-point operations per time-step becomes 2×10^{15} , which certainly requires 10Pflops-class supercomputers. Even with the K computer, though, it will be hard to follow the evolution of supernova cores over 1 s in 3D and such long-term simulations may be limited to axisymmetric 2D models. Nevertheless, the K computer makes it possible for us to accomplish systematic, high-resolution 2D Boltzmann simulations, which are still important on their own right.

To perform long-term 3D simulations by the 3D Boltzmann solver, on the other hand, we need supercomputers of Exaflops scale, which are expected to come as a next-generation platform. As shown in the table, the 3D neutrino radiation hydrodynamics simulations with a sufficient resolution will be feasible only if a memory of 3 PB is available and the computational speed is fast enough to handle 8×10^{16} operations per time-step. So far we have ignored inelastic scatterings, which would couple different energy grid points and increase the size of the dense sub-matrices by a factor of N_ϵ . Different energies are also coupled by Doppler effect and gravitational redshift, which are neglected in the current version of our Boltzmann solver. If these effects are taken into account and the resultant enlarged sub-matrices are to be inverted in the same way, the required memory and operation numbers are gigantic as given in the last row of the table, since they are proportional to N_ϵ^2 and N_ϵ^3 , respectively. Last but not least, the implementation of GR in the Boltzmann solver, the ultimate goal of our project, should be addressed at an appropriate point during this scale-up.

It is now obvious to readers that the supernova research is a subject of supercomputing science that keeps step with the advancement of hard and softwares for supercomputing. Hopefully, the next generation supercomputers will provide us with the opportunity to finally reach the goal. We hope also that our quest for the supernova mechanism will in turn contribute to pushing the limit of computational

science in the decade to come.

Acknowledgements

We are grateful to S. Furusawa, K. Nakazato, K. Kiuchi, N. Ohnishi and H. Suzuki for fruitful collaborations and profitable discussions on supernova simulations. KK, YS, and TT are grateful to K. Sato for continuing encouragements and also wish to thank their collaborators, W. Nakano-Iwakami, M. Liebendörfer, M. Hashimoto, S. Harikae, N. Yasutake, N. Nishimura, K. Nakamura, and K. Shaku. KS thanks Y. Sekiguchi for providing data from his 2D/3D simulations of core-collapse. We express our gratitude to C. Ott, A. Mezzacappa, H. -Th. Janka, E. Müller and W. Hillebrandt for valuable discussions on the current state-of-the-art simulations of supernovae. KS acknowledges the collaboration with H. Matsufuru, A. Imakura, T. Sakurai and S. Hashimoto and their advice on parallel computing.

The numerical computations in this work were performed in part on the supercomputers at the center for Computational Astrophysics, CfCA, the National Astronomical Observatory of Japan, Research Center for Nuclear Physics (RCNP) in Osaka University, The University of Tokyo, Yukawa Institute for Theoretical Physics (YITP) in Kyoto University, Japan Atomic Energy Agency (JAEA) and High Energy Accelerator Research Organization (KEK).

This work is partially supported by the Grant-in-Aid for Scientific Research on Innovative Areas (Nos. 20105004, 20105005) and the Grant-in-Aid for the Scientific Research (Nos. 19104006, 20740150, 21540281, 22540296, 23540323, and 23340069) from the Ministry of Education, Culture, Sports, Science and Technology (MEXT) in Japan.

The numerical study on core-collapse supernovae using the supercomputer facilities is supported by the HPCI Strategic Program of MEXT, Japan.

References

- 1) S. A. Colgate and R. H. White, *Astrophys. J.* **143** (1966), 626.
- 2) K. Kotake, K. Sato and K. Takahashi, *Rep. Prog. Phys.* **69** (2006), 971, arXiv:astro-ph/0509456.
- 3) K. Kotake, accepted to *Comptes Rendus Physique* (2012); arXiv:1110.5107.
- 4) Smartt, S. J. *Annual Review of Astronomy and Astrophysics* 47,2009,63
- 5) Utrobin, V. P. & Chugai, N. N. *Astron. Astrophys.* **532** (2011), A100
- 6) K. Sato and H. Suzuki, *Phys. Rev. Lett.* **58** (1987), 2722.
- 7) G. Raffelt, *Proceedings ISAPP School "Neutrino Physics and Astrophysics"*, 26 July-5 August 2011, Villa Monastero, Varenna, Italy; arXiv:1201.1637.
- 8) H. -Th. Janka, K. Langanke, A. Marek, G. Martínez-Pinedo and B. Müller, *Phys. Rep.* **442** (2007), 38.
- 9) J. R. Wilson, *Numerical Astrophysics* (1985), p422.
- 10) H. A. Bethe and J. R. Wilson, *Astrophys. J.* **295** (1985), 14.
- 11) M. Rampp and H.-Th. Janka, *Astrophys. J.* **539** (2000), L33.
- 12) M. Liebendörfer, A. Mezzacappa, F.-K. Thielemann, O. E. Messer, W. R. Hix and S. W. Bruenn, *Phys. Rev. D* **63** (2000), 103004.
- 13) T. A. Thompson, A. Burrows and P. A. Pinto, *Astrophys. J.* **592** (2003), 434.
- 14) K. Sumiyoshi, S. Yamada, H. Suzuki, H. Shen, S. Chiba and H. Toki, *Astrophys. J.* **629** (2005), 922.
- 15) C. J. Horowitz, *Phys. Rev. D* **65** (2002), 043001.

- 16) R. Buras, M. Rampp, H.-Th. Janka and K. Kifonidis, *Phys. Rev. Lett.* **90** (2003), 241101.
- 17) A. Burrows, S. Reddy and T. A. Thompson, *Nucl. Phys. A* **777** (2006), 356.
- 18) F. S. Kitaura, H.-Th. Janka and W. Hillebrandt, *Astron. Astrophys.* **450** (2006), 345.
- 19) L. Wang, D. A. Howell, P. Höflich and J. C. Wheeler, *Astrophys. J.* **550** (2001), 1030.
- 20) K. Maeda et al., *Science* **319** (2008), 1220.
- 21) M. Tanaka, K. S. Kawabata, K. Maeda, M. Iye, T. Hattori, E. Pian, K. Nomoto, P. A. Mazzali and N. Tominaga, *Astrophys. J.* **699** (2009), 1119.
- 22) M. Herant, W. Benz and S. Colgate, *Astrophys. J.* **395** (1992), 642.
- 23) T. Shimizu, S. Yamada and K. Sato, *Publ. Astron. Soc. J.* **45** (1993), L53.
- 24) A. Burrows, J. Hayes, & B. A. Fryxell, *Astrophys. J.* **450** (1995), 830.
- 25) H.-Th. Janka and E. Müller, *Astron. Astrophys.* **306** (1996), 167.
- 26) C. L. Fryer, *Astrophys. J.* **601** (2004), L175.
- 27) J. M. Blondin and A. Mezzacappa and C. DeMarino, *Astrophys. J.* **584** (2003), 971.
- 28) L. Scheck, K. Kifonidis, H.-T. Janka and E. Müller, *Astron. Astrophys.* **457** (2006), 963.
- 29) N. Ohnishi, K. Kotake and S. Yamada, *Astrophys. J.* **641** (2006), 1018, arXiv:astro-ph/0509765.
- 30) N. Ohnishi, K. Kotake and S. Yamada, *Astrophys. J.* **667** (2007), 375, arXiv:astro-ph/0606187.
- 31) T. Foglizzo, L. Scheck and H.-Th. Janka, *Astrophys. J.* **652** (2006), 1436.
- 32) W. Iwakami, K. Kotake, N. Ohnishi, S. Yamada and K. Sawada, *Astrophys. J.* **678** (2008), 1207, arXiv:0710.2191.
- 33) W. Iwakami, K. Kotake, N. Ohnishi, S. Yamada and K. Sawada, *Astrophys. J.* **700** (2009), 232, arXiv:0811.0651.
- 34) J. W. Murphy and A. Burrows, *Astrophys. J.* **688** (2008), 1159.
- 35) R. Fernández and C. Thompson, *Astrophys. J.* **703** (2009), 1464.
- 36) R. Buras, M. Rampp, H.-Th. Janka and K. Kifonidis, *Astron. Astrophys.* **447** (2006), 1049.
- 37) S. E. Woosley, A. Heger and T. A. Weaver, *Rev. Mod. Phys.* **74** (2002), 1015.
- 38) S. E. Woosley and T. A. Weaver, *Astrophys. J. Suppl.* **101** (1995), 181.
- 39) A. Marek and H.-Th. Janka, *Astrophys. J.* **694** (2009), 664.
- 40) S. W. Bruenn, A. Mezzacappa, W. R. Hix, J. M. Blondin, P. Marronetti, O. E. B. Messer, C. J. Dirk and S. Yoshida, *AIP Conference Proceedings* **180** (2009), pp. 1-5; arXiv:1002.4914.
- 41) M. Liebendörfer, S. C. Whitehouse and T. Fischer, *Astrophys. J.* **698** (2009), 1174.
- 42) Y. Suwa, K. Kotake, T. Takiwaki, S. C. Whitehouse, M. Liebendörfer and K. Sato, *Publ. Astron. Soc. J.* **62** (2010), L49, arXiv:0912.1157.
- 43) Kotake, K., Yamada, S., & Sato, K. 2003, *Astrophys. J.*, 595, 304
- 44) Y. Yamamoto and S. Yamada, "Formations of Compact Objects: from the cradle to the grave", March 7-9 (2012), Waseda Univ., <http://www.heap.phys.waseda.ac.jp/cnf1203/program.html>.
- 45) J. M. Lattimer and F. D. Swesty, *Nucl. Phys. A* **535** (1991), 331.
- 46) S. Shlomo, V. M. Kolomietz and G. Colò, *European Physical Journal A* **30** (2006), 23.
- 47) P. B. Demorest, T. Pennucci, S. M. Ransom, M. S. E. Roberts and J. W. T. Hessels, *Nature* **467** (2010), 1081.
- 48) E. O'Connor and C. D. Ott, *Astrophys. J.* **730** (2011), 70.
- 49) K. Kiuchi and K. Kotake, *MNRAS* **385** (2008), 1327, arXiv:0708.3597.
- 50) W. Hillebrandt, K. Nomoto and R. G. Wolff, *Astron. Astrophys.* **133** (1984), 175.
- 51) H.-Th. Janka, private communications.
- 52) Y. Suwa, "Formations of Compact Objects: from the cradle to the grave", March 7-9 (2012), Waseda Univ., <http://www.heap.phys.waseda.ac.jp/cnf1203/program.html>.
- 53) A. W. Steiner, J. M. Lattimer and E. F. Brown, *Astrophys. J.* **722** (2010), 33.
- 54) Lattimer, J. M., & Lim, Y. 2012, arXiv:1203.4286
- 55) J. M. Blondin and A. Mezzacappa, *Nature* **445** (2007), 58.
- 56) J. Nordhaus, A. Burrows, A. Almgren and J. Bell, *Astrophys. J.* **720** (2010), 694.
- 57) F. Hanke, A. Marek, B. Müller and H.-Th. Janka, submitted to *Astrophys. J.* (2011); arXiv:1108.4355.
- 58) A. Burrows, E. Livne, L. Dessart, C. D. Ott and J. Murphy, *Astrophys. J.* **640** (2006), 878.
- 59) N. N. Weinberg and E. Quataert, *MNRAS* **387** (2008), L64.

- 60) S. Yoshida, N. Ohnishi and S. Yamada, *Astrophys. J.* **665** (2007), 1268.
- 61) LeBlanc, J. M. & Wilson, J. R. 1970, *Astrophys. J.*, 161, 541 LeBlanc, J. M. & Wilson, J. R. 1970, *Astrophys. J.*, 161, 541
- 62) S. Yamada and H. Sawai, *Astrophys. J.* **608** (2004), 907.
- 63) Kotake, K., Sawai, H., Yamada, S., & Sato, K. 2004, *Astrophys. J.*, 608, 391
- 64) T. Takiwaki, K. Kotake, S. Nagataki and K. Sato, *Astrophys. J.* **616** (2004), 1086, arXiv:astro-ph/0408388.
- 65) K. Kotake, S. Yamada and K. Sato, *Astrophys. J.* **618** (2005), 474, arXiv:astro-ph/0409244.
- 66) K. Kotake, S. Yamada, K. Sato, K. Sumiyoshi, H. Ono and H. Suzuki, *Phys. Rev. D* **69** (2004), 124004, arXiv:astro-ph/0401563.
- 67) Suwa, Y., Takiwaki, T., Kotake, K., & Sato, K. 2007, *Astrophys. J. Lett.*, 665, L43
- 68) Suwa, Y., Takiwaki, T., Kotake, K., & Sato, K. 2007, *Pub. Astro. Soc. Japan*, 59, 771
- 69) T. Takiwaki, K. Kotake and K. Sato, *Astrophys. J.* **691** (2009), 1360, arXiv:0712.1949.
- 70) A. Burrows, L. Dessart, E. Livne, C. D. Ott and J. Murphy, *Astrophys. J.* **664** (2007), 416.
- 71) J. Guilet, T. Foglizzo and S. Fromang, *Astrophys. J.* **729** (2011), 71.
- 72) M. Obergaulinger and H.-Th. Janka, submitted to *Astron. Astrophys.* (2011); arXiv:1101.1198.
- 73) T. Takiwaki and K. Kotake, *Astrophys. J.* **743** (2011), 30, arXiv:1004.2896.
- 74) Kotake, K., Takiwaki, T., Suwa, Y., et al. 2012, arXiv:1204.2330
- 75) Endeve, E., Cardall, C. Y., Budiardja, R. D., et al. 2012, arXiv:1203.3108
- 76) S. Akiyama, J. C. Wheeler, D. L. Meier and I. Lichtenstadt, *Astrophys. J.* **584** (2003), 954.
- 77) S. -C. Yoon and N. Langer, *Astron. Astrophys.* **443** (2005), 643.
- 78) S. E. Woosley and A. Heger, *Astrophys. J.* **637** (2006), 914.
- 79) Z. B. Etienne, Y. T. Liu and S. L. Shapiro, *Phys. Rev. D* **74** (2006), 044030.
- 80) Obergaulinger, M., Cerdá-Durán, P., Müller, E., & Aloy, M. A. 2009, *Astron. Astrophys.*, 498, 241
- 81) M. Takahara and K. Sato, *Prog. Theor. Phys.* **80** (1988), 861.
- 82) I. Sagert, T. Fischer, M. Hempel, G. Pagliara, J. Schaffner-Bielich, A. Mezzacappa, F. Thielemann and M. Liebendörfer, *Phys. Rev. Lett.* **102** (2009), 081101.
- 83) T. Fischer, I. Sagert, G. Pagliara, M. Hempel, J. Schaffner-Bielich, T. Rauscher, F.-K. Thielemann, R. Käppeli, G. Martínez-Pinedo and M. Liebendörfer, *Astrophys. J. Suppl.* **194** (2011), 39.
- 84) T. A. Thompson, E. Quataert and A. Burrows, *Astrophys. J.* **620** (2005), 861.
- 85) Y. Masada, T. Takiwaki and K. Kotake, submitted to *Astrophys. J.* (2011).
- 86) T. K. Suzuki, K. Sumiyoshi and S. Yamada, *Astrophys. J.* **678** (2008), 1200.
- 87) H. Shen, H. Toki, K. Oyamatsu and K. Sumiyoshi, *Nucl. Phys. A* **637** (1998), 435.
- 88) H. Shen, H. Toki, K. Oyamatsu and K. Sumiyoshi, *Prog. Theor. Phys.* **100** (1998), 1013.
- 89) H. Shen, H. Toki, K. Oyamatsu and K. Sumiyoshi, *Astrophys. J. Suppl.* **197** (2011), 20.
- 90) M. Hempel and J. Schaffner-Bielich, *Nucl. Phys. A* **837** (2010), 210.
- 91) S. Furusawa, S. Yamada, K. Sumiyoshi and H. Suzuki, *Astrophys. J.* **738** (2011), 178.
- 92) G. Shen, C. J. Horowitz and S. Teige, *Phys. Rev. C* **83** (2011), 035802.
- 93) C. Ishizuka, A. Ohnishi, K. Tsubakihara, K. Sumiyoshi and S. Yamada, *J. of Phys.* **G35** (2008), 085201.
- 94) K. Nakazato, K. Sumiyoshi and S. Yamada, *Astrophys. J.* **721** (2010), 1284.
- 95) K. Nakazato, K. Sumiyoshi, H. Suzuki and S. Yamada, *Phys. Rev. D* **81** (2010), 083009.
- 96) K. Sumiyoshi, S. Yamada, H. Suzuki and S. Chiba, *Phys. Rev. Lett.* **97** (2006), 091101.
- 97) T. Fischer, S. C. Whitehouse, A. Mezzacappa, F.-K. Thielemann and M. Liebendörfer, *Astron. Astrophys.* **499** (2009), 1.
- 98) S. Furusawa, S. Yamada, K. Sumiyoshi and H. Suzuki, (2012) in preparation.
- 99) A. S. Botvina and I. N. Mishustin, *Nucl. Phys. A* **843** (2010), 98.
- 100) Woosley, S. E. & Bloom, J. S. *Annual Review of Astronomy and Astrophysics* 44,2006,507
- 101) Modjaz, M. 2011, *Astronomische Nachrichten*, 332, 434
- 102) H. Janka and E. Müller, *Astron. Astrophys.* **306** (1996), 167.
- 103) A. Wongwathanarat, N. J. Hammer and E. Müller, *Astron. Astrophys.* **514** (2010), A48.
- 104) E. Rantsiou, A. Burrows, J. Nordhaus and A. Almgren, *Astrophys. J.* **732** (2011), 57.

- 105) R. Fernández, *Astrophys. J.* **725** (2010), 1563.
- 106) E. Endeve, C. Y. Cardall, R. D. Budiardja and A. Mezzacappa, *Astrophys. J.* **713** (2010), 1219.
- 107) K. Kotake, W. Iwakami, N. Ohnishi and S. Yamada, *Astrophys. J.* **697** (2009), L133, arXiv:0904.4300.
- 108) E. Müller, H.-Th. Janka and A. Wongwathanarat, *Astron. Astrophys.* **537** (2012), 63.
- 109) H. Duan and J. P. Kneller, *J. of Phys.* **G36** (2009), 113201.
- 110) T. Takiwaki, K. Kotake and Y. Suwa, accepted to *ApJ* 2011; arXiv:1108:3989.
- 111) A. Burrows and J. Goshy, *Astrophys. J.* **416** (1993), L75.
- 112) H.-Th. Janka, *Astron. Astrophys.* **368** (2001), 527.
- 113) M. M. May and R. H. White, *Phys. Rev. Lett.* **141** (1966), 1232.
- 114) C. W. Misner and D. H. Sharp, *Phys. Rev.* **136** (1964), 571.
- 115) R. A. Schwartz, *Annals of Physics* **43** (1967), 42.
- 116) R. W. Lindquist, *Annals of Physics* **37** (1966), 487.
- 117) J. R. Wilson, *Astrophys. J.* **163** (1971), 209.
- 118) K. A. van Riper, *Astrophys. J.* **232** (1979), 558.
- 119) K. A. van Riper and J. M. Lattimer, *Astrophys. J.* **249** (1981), 270.
- 120) K. A. van Riper, *Astrophys. J.* **257** (1982), 793.
- 121) S. W. Bruenn, K. R. De Nisco and A. Mezzacappa, *Astrophys. J.* **560** (2001), 326.
- 122) S. W. Bruenn, *Astrophys. J. Suppl.* **58** (1985), 771.
- 123) A. Mezzacappa and S. W. Bruenn, *Astrophys. J.* **405** (1993), 669.
- 124) A. Mezzacappa and S. W. Bruenn, *Astrophys. J.* **410** (1993), 740.
- 125) S. Yamada, *Astrophys. J.* **475** (1997), 720.
- 126) S. Yamada, H.-T. Janka and H. Suzuki, *Astron. Astrophys.* **344** (1999), 533.
- 127) E. J. Lentz, A. Mezzacappa, O. E. Bronson Messer, M. Liebendörfer, W. R. Hix and S. Bruenn, *Astrophys. J.* in press (2012); arXiv:1112.3595.
- 128) R. Buras, H.-Th. Janka, M. Rampp and K. Kifonidis, *Astron. Astrophys.* 457 (2006), 281.
- 129) M. Shibata and Y. Sekiguchi, *Phys. Rev. D* **71** (2005), 024014.
- 130) M. Shibata and Y. Sekiguchi, *Phys. Rev. D* **72** (2005), 044014.
- 131) C. D. Ott, H. Dimmelmeier, A. Marek, H.-T. Janka, I. Hawke, B. Zink and E. Schnetter, *Phys. Rev. Lett.* **98** (2007), 261101.
- 132) H. Dimmelmeier, J. A. Font and E. Müller, *Astron. Astrophys.* **388** (2002), 917.
- 133) Cordero-Carrión, I., Cerdá-Durán, P., & Ibáñez, J. M, *Phys. Rev. D* **85** (2012), 044023
- 134) M. Liebendörfer, *Astrophys. J.* **633** (2005), 1042.
- 135) Y. Sekiguchi, *Prog. Theor. Phys.* **124** (2010), 331.
- 136) Ott, C. D., Abdikamalov, E., O'Connor, E., et al. 2012, arXiv:1204.0512
- 137) B. Müller, H.-T. Janka and A. Marek, submitted to *Astrophys. J.* (2012); arXiv:1202.0815.
- 138) B. Müller, H.-T. Janka and H. Dimmelmeier, *Astrophys. J. Suppl.* **189** (2010), 104.
- 139) T. Kuroda, K. Kotake and T. Takiwaki, accepted to *Astrophys. J.* (2012); arXiv:1202.2487.
- 140) T. Kuroda and H. Umeda, *Astrophys. J. Suppl.* **191** (2010), 439.
- 141) M. Shibata and T. Nakamura, *Phys. Rev. D* **52** (1995), 5428.
- 142) T. W. Baumgarte and S. L. Shapiro, *Phys. Rev. D* **59** (1999), 024007.
- 143) K. S. Thorne, *MNRAS* **194** (1981), 439.
- 144) M. Shibata, K. Kiuchi, Y. Sekiguchi and Y. Suwa, *Prog. Theor. Phys.* **125** (2011), 1255.
- 145) T. Foglizzo and M. Tagger, *Astron. Astrophys.* **363** (2000), 174.
- 146) T. Foglizzo, *Astron. Astrophys.* **392** (2000), 353.
- 147) L. Scheck, H.-Th. Janka, T. Foglizzo and K. Kifonidis, *Astron. Astrophys.* **477** (2008), 931.
- 148) M. Liebendörfer, O. E. B. Messer, A. Mezzacappa, S. W. Bruenn, C. Y. Cardall and F.-K. Thielemann, *Astrophys. J. Suppl.* **150** (2004), 263.
- 149) K. Kotake, W. Iwakami, N. Ohnishi and S. Yamada, *Astrophys. J.* **704** (2009), 951, arXiv:0909.3622.
- 150) K. Kotake, W. Iwakami-Nakano and N. Ohnishi, *Astrophys. J.* **736** (2011), 124, arXiv:1106.0544.
- 151) C. D. Ott, C. Reisswig, E. Schnetter, E. O'Connor, U. Sperhake, F. Löffler, P. Diener, E. Abdikamalov, I. Hawke, A. Burrows, *Phys. Rev. Lett.* **106** (2011), 161103.

- 152) R. Abbasi, Y. Abdou, T. Abu-Zayyad et al., *Astron. Astrophys.* **535** (2011), A109.
- 153) A. Marek, H.-Th. Janka and E. Müller, *Astron. Astrophys.* **496** (2009), 475.
- 154) T. Lund, A. Marek, C. Lunardini, H.-T. Janka and G. Raffelt, *Phys. Rev. D* **82** (2010), 063007.
- 155) S. Fujimoto, K. Kotake, M. Hashimoto, M. Ono and N. Ohnishi, *Astrophys. J.* **738** (2011), 61, arXiv:1106.2606.
- 156) F.-K. Thielemann, A. Arcones, R. Käppeli, M. Liebendörfer, T. Rauscher, C. Winteler, C. Fröhlich, I. Dillmann, T. Fischer, G. Martínez-Pinedo, K. Langanke, K. Farouqi, K.-L. Kratz, I. Panov and I. K. Korneev, *Prog. Part. Nucl. Phys.* **66** (2011), 346.
- 157) H. Suzuki, in *Physics and Astrophysics of Neutrinos* (1994), (eds. M. Fukugita and A. Suzuki, Springer-Verlag, Tokyo) p.763.
- 158) K. Sumiyoshi and S. Yamada, *Astrophys. J. Suppl.* **199** (2012), 17.
- 159) A. Mezzacappa, M. Liebendörfer, O. E. B. Messer, W. R. Hix, F.-K. Thielemann, S. W. Bruenn, *Phys. Rev. Lett.* **86** (2001), 1935.
- 160) M. Rampp and H.-Th. Janka, *Astron. Astrophys.* **396** (2002), 361.
- 161) M. Liebendörfer, A. Mezzacappa and F.-K. Thielemann, *Phys. Rev. D* **63** (2001), 103004.
- 162) K. Langanke, G. Martínez-Pinedo, J. M. Sampaio, D. J. Dean, W. R. Hix, O. E. B. Messer, A. Mezzacappa, M. Liebendörfer, H.-Th. Janka and M. Rampp, *Phys. Rev. Lett.* **90** (2003), 241102.
- 163) W. R. Hix, O. E. B. Messer, A. Mezzacappa, M. Liebendörfer, J. M. Sampaio, K. Langanke, D. J. Dean and G. Martínez-Pinedo, *Phys. Rev. Lett.* **91** (2003), 201102.
- 164) K. Sumiyoshi, S. Yamada and H. Suzuki, *Astrophys. J.* **667** (2007), 382.
- 165) T. Fischer, S. C. Whitehouse, A. Mezzacappa, F.-K. Thielemann and M. Liebendörfer, *Astron. Astrophys.* **517** (2010), A80.
- 166) T. Totani, K. Sato, H. E. Dalhed and J.R. Wilson, *Astrophys. J.* **496** (1998), 216.
- 167) S. Ando, J. F. Beacom and H. Yüksel, *Phys. Rev. Lett.* **95** (2005), 171101.
- 168) J. G. Keehn and C. Lunardini, *Phys. Rev. D* **85** (2012), 043011.
- 169) R. Walder, A. Burrows, C. D. Ott, E. Livne, I. Lichtenstadt and M. Jarrah, *Astrophys. J.* **626** (2005), 317.
- 170) E. Livne, A. Burrows, R. Walder, I. Lichtenstadt and T. A. Thompson, *Astrophys. J.* **609** (2004), 277.
- 171) check below
- 172) C. D. Ott, A. Burrows, L. Dessart and E. Livne, *Astrophys. J.* **685** (2008), 1069.
- 173) T. D. Brandt, A. Burrows, C. D. Ott and E. Livne, *Astrophys. J.* **728** (2011), 8.
- 174) J. M. Blondin and S. Shaw, *Astrophys. J.* **656** (2007), 366.
- 175) M. Hempel, T. Fischer, J. Schaffner-Bielich and M. Liebendörfer, *Astrophys. J.* **748** (2012), 70.
- 176) K. Sumiyoshi, S. Yamada and H. Suzuki *Astrophys. J.* **688** (2008), 1176.
- 177) K. Sumiyoshi, C. Ishizuka, A. Ohnishi, S. Yamada and H. Suzuki, *Astrophys. J.* **690** (2009), L43.
- 178) K. Nakazato, S. Furusawa, K. Sumiyoshi, A. Ohnishi, S. Yamada and H. Suzuki, *Astrophys. J.* **745** (2011), 197.
- 179) F. D. Swesty, J. M. Lattimer and E. S. Myra, *Astrophys. J.* **425** (1994), 195.
- 180) S. I. Blinnikov, I. V. Panov, M. A. Rudzsky and K. Sumiyoshi, *Astron. Astrophys.* **535** (2011), A37.
- 181) C. L. Fryer, *Astrophys. J.* **522** (1999), 413.
- 182) K. Maeda and K. Nomoto, *Astrophys. J.* **598** (2003), 1163.
- 183) K. Nomoto, *ASP Conf. Ser.* **332** (2005), 374; arXiv:astro-ph/0506597.
- 184) K. Nakazato, K. Sumiyoshi, H. Suzuki and S. Yamada, *Phys. Rev. D* **78** (2008), 083014.
- 185) K. Abe et al. Letter of Intent (2011), arXiv:1109.3262.
- 186) M. D. Kistler, H. Yüksel, S. Ando, J. F. Beacom and Y. Suzuki, *Phys. Rev. D* **83** (2011), 123008.
- 187) K. Sumiyoshi and T. Ebisuzaki, *Parallel Computing* **24** (1998), 287.
- 188) D. Mihalas and B. W. Mihalas, *Foundations of Radiation Hydrodynamics* (Dover Publications, 1999).
- 189) Abdikamalov, E., Burrows, A., Ott, C. D., et al. 2012, arXiv:1203.2915
- 190) H. Nagakura, K. Sumiyoshi and S. Yamada, in preparation.
- 191) S. E. Woosley, in *Gamma-ray Bursts* (eds. C. Kouveliotou, S. E. Woosley and R. A. M.

- J. Wijers, Cambridge University Press, 2012); arXiv:1105.4193.
- 192) A. I. MacFadyen, S. E. Woosley and A. Heger, *Astrophys. J.* **550** (1999), 410.
 - 193) Paczynski, B. 1990, *Astrophys. J.*, 363, 218
 - 194) Meszaros, P. & Rees, M. J. 1992, *MNRAS*, 257, 29P
 - 195) S. Harikae, K. Kotake and T. Takiwaki, *Astrophys. J.* **713** (2010), 304, arXiv:0912.2590.
 - 196) I. Zalamea and A. M. Beloborodov, *MNRAS* **410** (2011), 2302.
 - 197) Fujimoto, S.-i., Hashimoto, M.-a., Kotake, K., & Yamada, S. 2007, *Astrophys. J.*, 656, 382
 - 198) Ono, M., Hashimoto, M., Fujimoto, S., Kotake, K., & Yamada, S. 2009, *Progress of Theoretical Physics*, 122, 755
 - 199) Ono, M., Hashimoto, M.-a., Fujimoto, S.-i., Kotake, K., & Yamada, S. 2012, arXiv:1203.6488
 - 200) Winteler, C., Kaeppli, R., Perego, A., et al. 2012, arXiv:1203.0616
 - 201) Ruffert, M., Janka, H.-T., Takahashi, K., & Schaefer, G. 1997, *Astron. Astrophys.*, 319, 122
 - 202) Ruffert, M. & Janka, H.-T. 1998, *Astron. Astrophys.*, 338, 535
 - 203) Birkel, R., Aloy, M. A., Janka, H.-T., & Müller, E. 2007, *Astron. Astrophys.*, 463, 51
 - 204) Harikae, S., Kotake, K., Takiwaki, T., & Sekiguchi, Y.-i. 2010, *Astrophys. J.*, 720, 614
 - 205) Kotake, K., Takiwaki, T., Harikae, S, accepted to *Astrophys. J.* (2012); arXiv:1205.6061
 - 206) Dessart, L., Ott, C. D., Burrows, A., Rosswog, S., & Livne, E. 2009, *Astrophys. J.*, 690, 1681
 - 207) Y. Sekiguchi and M. Shibata, *Astrophys. J.* **737** (2011), 6.
 - 208) Y. Saad, *Iterative Methods for Sparse Linear Systems*, 2nd Edition (Philadelphia, PA: SIAM, 2003).
 - 209) R. Barrett et al., *Templates for the Solution of Linear Systems: Building Blocks for Iterative Methods*, 2nd Edition (Philadelphia, PA: SIAM, 1994)
 - 210) A. Imakura, T. Sakurai, H. Matsufuru and K. Sumiyoshi, (2012) in preparation.